Received: 26 May 2025 | Revised: 16 January 2026 | Accepted: 31 March 2026

DOI: 10.1002/qj.70199

Quarterly Journal of the Royal Meteorological Society RMetS

RESEARCH ARTICLE

Lagrangian analysis of two flavours of Central European heatwaves: Formation under omega blocking versus initiation by subtropical ridges

Alexander Lemburg[1] | **Andreas H. Fink**[1] | **Miguel M. Lima**[2] | **Joaquim G. Pinto**[1]

[1]Institute for Meteorology and Climate Research—Troposphere Research (IMKTRO), Karlsruhe Institute of Technology (KIT), Karlsruhe, Germany

[2]Instituto Dom Luiz (IDL), Faculdade de Ciências, Universidade de Lisboa, Lisbon, Portugal

Correspondence
Alexander Lemburg, Karlsruhe Institute of Technology (KIT), Institute for Meteorology and Climate Research—Troposphere Research (IMKTRO), Karlsruhe, Germany.
Email: alexander.lemburg@kit.edu

Funding information
Bundesministerium für Forschung, Technologie und Raumfahrt, Grant/Award Number: ClimXtreme II (01LP2322A); AXA Research Fund; PhD MIT Portugal MPP2030-FCT, Grant/Award Number: 10.54499/PRT/BD/154680/2023

Abstract

The formation of midlatitude heatwaves (HWs) is closely linked to quasi-stationary anticyclonic flow anomalies, which are often associated with so-called omega blocking. However, not all HWs require atmospheric blocking, especially over Southern and Central Europe, where they can also be enabled by poleward extensions of the subtropical high-pressure belt. We propose that HWs forming under omega blocking may differ in Lagrangian characteristics from those related to subtropical ridges, in terms of both air-mass origin and processes warming air parcels en route to Central Europe. With this aim, we select the 25 most archetypical cases of omega- and ridge-type Central European HWs, respectively, during the period 1950–2023. Using ERA5-based backward trajectories and a Lagrangian temperature decomposition, we assess both air-mass origin and the relative importance of the heat-generating processes: advection, adiabatic warming through subsidence, and diabatic heating. Our analysis shows that adiabatic warming and diabatic heating are the dominant near-surface heat-generating processes for both circulation types. Advection does not contribute to omega-type HWs, while ridge-type HWs show small but significant contributions by advection, as air masses originate from more southern, climatologically warmer regions. Adiabatic warming is more significant in ridge-type HWs, while omega-type HWs see a significantly stronger role of diabatic heating due to a combination of less diabatic cooling in the free troposphere and longer air-mass residence in the boundary layer. At higher levels (~800 hPa), high temperatures are only attributable to advection and adiabatic warming. Significant differences between both circulation types emerge only two days after HW onset, when advection becomes dominant and significantly more important in ridge-type HWs than in omega-type HWs. These results highlight the importance of the atmospheric circulation and thus the associated air masses to the development of HWs, with implications for both weather forecasting and climate-change perspectives.

KEYWORDS

atmospheric ridges, blocking, dynamical meteorology, Europe, heatwaves

1 | INTRODUCTION

With globally rising temperatures, heat extremes pose an ever-increasing burden on human health as well as economical and ecological systems (Legg, 2021). Among the many regions of the globe affected, Europe has become a hot spot for unprecedented heat extremes (Kornhuber *et al.*, 2024). Compared with the rest of the northern mid-latitudes, European heat extremes have increased three to four times faster over the past four decades (Dong & Sutton, 2025; Rousi *et al.*, 2022). Prominent examples encompass August 2003 (Fink *et al.*, 2004; García-Herrera *et al.*, 2010), the summer of 2010 in Eastern Europe and Western Russia (Barriopedro *et al.*, 2011), or the ongoing series of anomalously dry and hot summers starting in 2018 (Kueh & Lin, 2020; Rousi *et al.*, 2023; Sousa *et al.*, 2020). The accelerated trend in heat extremes over Europe has been linked to both regional thermodynamic drivers, such as aerosol reductions (Dong & Sutton, 2025; Schumacher *et al.*, 2024) or changes in early summer soil moisture (Stegehuis *et al.*, 2021), and changes in the large-scale atmospheric circulation (Rousi *et al.*, 2022; Singh *et al.*, 2023; Vautard *et al.*, 2023).

In many parts of Europe, the formation of a heatwave (HW) is usually linked to an anomalous large-scale atmospheric circulation characterized by the lasting presence of high-pressure systems over the same region (Alvarez-Castro *et al.*, 2018; Kautz *et al.*, 2022; Kueh & Lin, 2020; Pfahl & Wernli, 2012; Schaller *et al.*, 2018). Such quasi-stationary anticyclonic flow anomalies, often accompanied by a substantial weakening or displacement of the westerly flow, are usually referred to as atmospheric blocking. The onset of a blocking event is generally initiated by the amplification or breaking of Rossby waves. Atmospheric blocking comes in different flavours as well as temporal stages. Using the potential vorticity (PV) perspective, one can separate the earlier stages of blocking formation, in which PV contours are more and more displaced meridionally but not yet overturned, from the later wave-breaking stage, in which an irreversible overturning of PV contours leads to a flow reversal (Woollings *et al.*, 2018). During summer, atmospheric blocking often takes on a characteristic omega shape, where a relatively widespread area of anomalously high pressure is flanked by low-pressure systems to the west and east. The jet stream is displaced substantially poleward, but the area of anomalously high pressure or geopotential is not fully secluded from the subtropical high-pressure belt and there is generally no complete flow reversal.[1]

Although there is a non-disputable statistical relationship for most parts of Europe, the presence of atmospheric blocking is not always a necessary precondition for HW formation. In the more southern regions of Europe, particularly over Iberia, HWs or droughts are often already enabled by poleward extensions of the subtropical high-pressure belt (García-Herrera *et al.*, 2005; Sánchez-Benítez *et al.*, 2020; Santos *et al.*, 2009; Sousa *et al.*, 2019). In contrast to a pronounced atmospheric blocking, subtropical ridges mostly feature no wave breaking and are characterized by rather small distortions of potential vorticity contours and comparably weak anomalies in the mean westerly flow (Sousa *et al.*, 2021). Such differences in the large-scale flow environment might also imprint on the conditions near the surface. We therefore hypothesize that the processes leading to heat may also differ between omega-type and ridge-type heatwaves.

In general, anticyclones are associated with large-scale subsidence of air masses, which can contribute substantially to extreme temperatures in summer. Moreover, the widespread subsidence suppresses cloud formation, which will strengthen the diabatic heating of near-surface air masses, particularly if evapotranspiration is low due to desiccated soils. Finally, the onset of a HW in particular may feature the transport of a climatologically much warmer air mass into the focus region. In many parts of Europe, all three processes—subsidence, diabatic heating and advection—may contribute positively to HW formation from a climatological perspective (Röthlisberger & Papritz, 2023). However, quantitatively, the two former processes, particularly adiabatic warming due to subsidence, are usually the most important in explaining the generation of anomalous near-surface heat. In line with this, other authors have attributed rather little importance to advection (Bieli *et al.*, 2015; Zschenderlein *et al.*, 2019). However, depending on the exact focus region and also the methods used, there is a high case-to-case variability, where for individual HWs any single process or a mix of two processes may be identified as clearly dominant (Santos *et al.*, 2015; Zschenderlein *et al.*, 2018). For instance, the first bout of extreme heat in western Europe in June 2019 was shown to be strongly associated with warm-air advection, whereas the subsequent heatwave in July has been linked more to local diabatic processes (Sousa *et al.*, 2020).

While the high case-to-case variability might be related to a number of causes, we hypothesize that the individual relative importance of subsidence, diabatic heating, and advection might be related systematically to the type of atmospheric flow anomaly that enables the HW formation. Ultimately, the respective roles of these processes will also be closely linked to the origin of the air masses involved and their respective pathways and the diabatic processes they undergo until arrival in the region of interest. While not focusing on heatwaves per se, Sousa *et al.* (2018) have pioneered the idea of studying the role

of the aforementioned three temperature-modulating processes conditioned on the prevalent flow type of either blocking or ridge presence.

In this article, we seek to build upon and extend the previous work of Sousa *et al.* (2018). Using a Lagrangian approach, as in Röthlisberger and Papritz (2023), we aim to achieve a deeper understanding of the relative importance of heat-producing processes in Central European HWs and their link to the large-scale flow by asking the following three questions.

- Where do air masses involved in Central European HWs usually come from and are there substantial differences between HWs associated with an omega blocking and those initiated by subtropical ridges?
- Does the relative importance of the processes of advection, adiabatic warming, and diabatic warming differ fundamentally between ridge- and omega-type HWs and does the relative importance of these processes change over the course of the heatwave?
- Is there a substantial difference in terms of how diabatic processes in both the free troposphere and the planetary boundary layer affect the air masses involved?

We aim to answer these questions within a Lagrangian framework by computing backward trajectories for the 25 most archetypical cases of Central European HWs forming either under an omega-type blocking or under a subtropical ridge, respectively. These cases are identified with the help of the detection algorithm of Sousa *et al.* (2021), which distinguishes between multiple types of blocking and subtropical ridges. By applying the Lagrangian temperature anomaly decomposition algorithm of Röthlisberger and Papritz (2023), we then quantify the origin and pathway of air masses and the average relative importance of the processes of advection, adiabatic warming due to subsidence, and diabatic heating. Doing so, we expand the works of Röthlisberger and Papritz (2023) in three ways. First, we are able to stratify the importance of heat-generating processes by the type of large-scale flow anomaly present. Secondly, by using selected cases of multi-day HWs for which we can initiate trajectories in different stages, we are able to obtain a deeper understanding of how the relevant processes causing heat may change over the course of a heatwave. Finally, we also apply the analysis described above to trajectories initiated from a level slightly above the boundary layer to test how strongly the relative importance of processes leading to anomalous heat differs from the near-surface case.

This article is structured as follows. In Section 2, we outline both the data and the multiple methods used in this article. In Section 3, we show the results of the Lagrangian investigation into the 25 most archetypical omega and subtropical ridge cases of Central European HWs. For air masses started both near the surface and around the top of the planetary boundary layer, we assess the average origin and pathway of air masses and quantify the relative importance of the processes of advection, adiabatic warming, and diabatic warming. Finally, Section 4 contains a summary and discussion of the findings of this study and puts them into the context of previous, current, and suggested further research.

2 | DATA AND METHODS

This section first introduces the data and outlines our study case selection based on the objective detection of HWs as well as the identification and distinction between omega blocking and subtropical ridges. Thereafter follows a detailed description of the technique with which the relative importance of the heat-inducing processes is assessed, which is based on backward trajectories with Lagranto and the subsequent application of the algorithm of Röthlisberger and Papritz (2023). For a better overview, the entire workflow is presented as a flow chart in Figure 1.

2.1 | Data

For all analyses, we use ERA5 reanalysis data (Soci *et al.*, 2024), based on four-dimensional variational (4D-Var) data assimilation and short forecasts of the European Centre for Medium-Range Weather Forecasts (ECMWF) Integrated Forecasting System (IFS) Cycle 41r2. Data are available at an hourly temporal resolution, a spatial resolution of about 31 km, and a vertical resolution of 137 model levels. Table 1 lists all variables used in this article and details the spatial and temporal resolutions used, which depend on the respective method. Our time period of interest for all analyses consists of the summer months from May to the end of September during years 1950–2023.

2.2 | HW detection

In the Central European focus region, HWs with a length of three or more days are detected via an objective algorithm, using the same technique as in Lemburg and Fink (2024). In a first step, time series of daily maximum 2-m temperature are obtained from hourly ERA5 data at 1° spatial resolution for each grid point within a rectangular box spanning 4°E–16°E and 48°N–55°N (red rectangle in Figure 2a). Following a linear detrending of

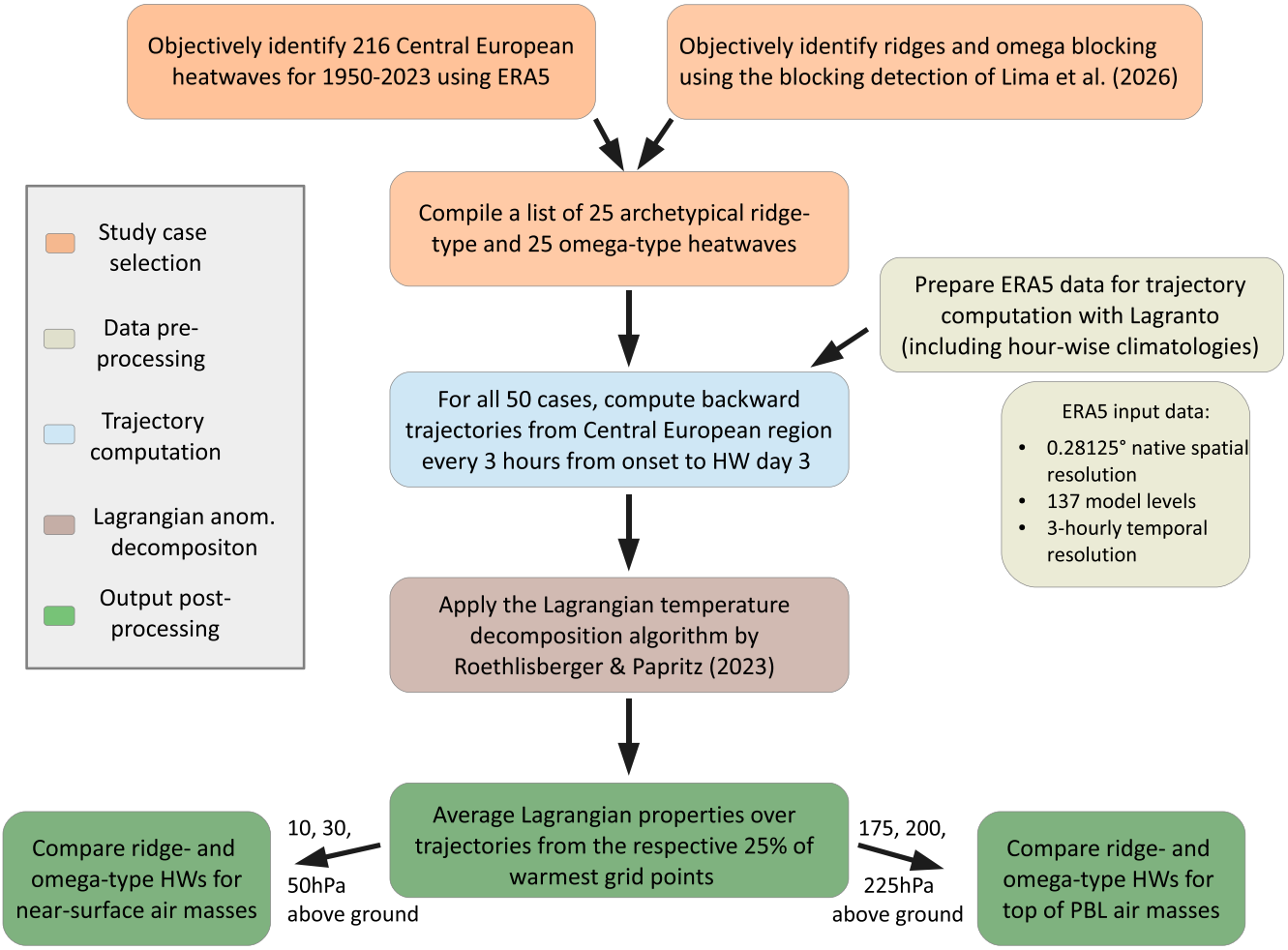

FIGURE 1 Flow chart outlining the workflow used in this article to analyse the different Lagrangian characteristics of ridge- and omega-type Central European heatwaves. [Colour figure can be viewed at wileyonlinelibrary.com]

these time series, grid-point wise daily maximum temperature anomalies are computed with respect to a smoothed daily climatology. Those anomalies are standardized further by the local standard deviation to account for typical year-to-year variations at any given location. The subsequent HW detection is outlined schematically with an example in Figure 2b. The algorithm first searches for all grid points where the 90th percentile of the daily anomaly time series obtained is exceeded and then integrates the daily standardized temperature anomalies spatially over the entire domain. If the regional sum of standardised anomalies weighted by the cosine of latitude also surpasses its respective 90th percentile for at least three consecutive days, the respective event is identified as a regional HW with a clearly defined onset and decay date. Over the period of 1950–2023, we identify 216 Central European HWs with this method. For each HW, we further define a magnitude reflecting its intensity, duration, and spatial extent by integrating spatially and temporally over the standardized anomalies.

2.3 | Blocking detection

In this article, we use a blocking and ridge-detection algorithm first presented in Sousa *et al.* (2021) and modified recently in Lima *et al.* (2026). The core of the detection algorithm builds upon previous work by Tibaldi and Molteni (1990), with the key metric being the 500-hPa geopotential height ($Z500$) and its latitudinal gradient. One of the additional features of the algorithm of Sousa *et al.* (2021) is the detection of the subtropical high-pressure belt. This is, by definition, the latitude at which the instantaneous local $Z500$ value is higher than the hemisphere-wide mean value averaged over the previous 15 days. In the updated version we are using, this latitude, marking the extent of the subtropical high-pressure belt called LAT_{min}, is now also a function of longitude, which allows us to account better for quasi-stationary ridges. North of LAT_{min}, blocking will then be identified for individual grid cells by computing both the northward- and southward-directed meridional

TABLE 1 Overview of all variables used in this study, stating their purpose as well as the different temporal and spatial resolutions.

Variable	Acronym	Purpose	Temp. resol.	Spat. resol.	Vert. levels
2-m maximum temperature	mx2t	HW detection	Daily	1°	1 (2 m)
500-hPa geopotential	*z*	Ridge/Omega detection	Daily	1°	1 (500 hPa)
Temperature	*t*	Trajectory comp.	three-hourly	0.28125°	137 model levs
Potential temperature (computed)		Trajectory comp.	three-hourly	0.28125°	137 model levs
Pressure	*p*	Trajectory comp.	three-hourly	0.28125°	137 model levs
Zonal wind	*u*	Trajectory comp.	three-hourly	0.28125°	137 model levs
Meridional wind	*v*	Trajectory comp.	three-hourly	0.28125°	137 model levs
Vertical wind (omega)	*w*	Trajectory comp.	three-hourly	0.28125°	137 model levs
Surface pressure	sp	Trajectory comp.	three-hourly	0.28125°	1 (surf.)
Geometric height (computed)		Traced variable	three-hourly	0.28125°	137 model levs
Planetary boundary-layer height	blh	Traced variable	three-hourly	0.28125°	–
Surface down. short-wave rad.	ssrd	Traced variable	three-hourly	0.28125°	1 (surf.)
Vol. soil moisture level 1	swvl1	Traced variable	three-hourly	0.28125°	1 (soil; 0–7 cm)
Land–sea mask	lsm	Traced variable	–	0.28125°	–

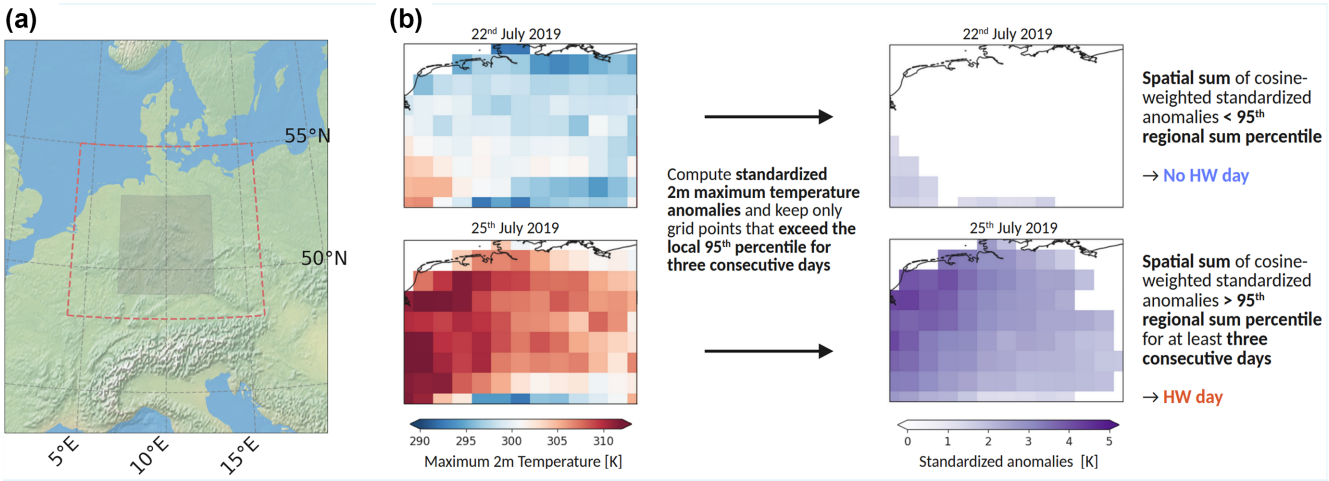

FIGURE 2 Overview of the study area and schematic depiction of the HW detection algorithm. (a) In the map, the red rectangle depicts the domain used for the detection of Central European HWs, whereas the grey shading depicts the area from which trajectories are initiated. (b) Schematic description of the HW detection algorithm applied for the example of the July 2019 heatwave. [Colour figure can be viewed at wileyonlinelibrary.com]

*Z*500 gradients, in form of geopotential meters (gpm) per degree, over a latitudinal span of 15°, respectively. If the northern gradient is below 0 gpm/° and the southern gradient exceeds 0 gpm/°, the respective local grid point is flagged as blocked.

After the local and instantaneous detection, the algorithm groups spatially contiguous grid points poleward of LAT_{min} into structures, irrespective of the individual grid-point wise assignments. Finally, subtropical ridges are identified as either all those structures that cover less than 500,000 km^2 blocked area or those structures that extend less than 15° poleward of LAT_{min}. Otherwise, the structure is classified as a blocking. The further distinction between omega and Rex-type blocking is based on additional criteria as described in Lima *et al.* (2026), but, as mentioned earlier, Rex is very rarely detected in the midlatitudes during boreal summer.

The rationale of using the blocking and ridge-detection algorithm of Sousa *et al.* (2021) can be given by means of two examples. The first row of Figure 3 features a heatwave associated with an archetypical omega blocking, which can also be easily confirmed visually by means of the

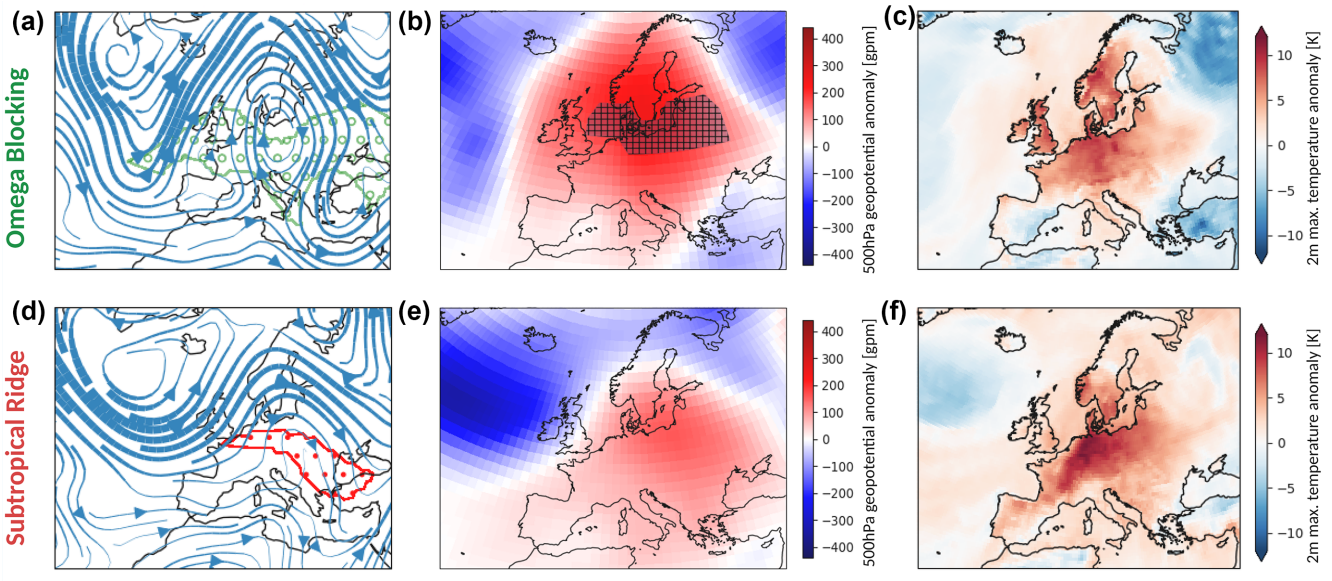

FIGURE 3 Example cases of HWs associated with two different flavours of large-scale flow anomalies. The first columns presents the large-scale flow in the form of streamlines based on 500-hPa daily mean winds for (a) June 1, 1982, a selected case with archetypical omega blocking, and (d) September 18, 2018, a case with an archetypical ridge-type HW. Areas with coloured markers denote different types of atmospheric blocking as detected by the Sousa *et al.* (2021) algorithm, with green denoting omega blocking and red showing subtropical ridges (other types not present in these examples). The second column (b, e) shows corresponding anomalies in 500-hPa geopotential with respect to a smoothed running climatology. In contrast to the first column, the black stippling marks areas where the algorithm of Scherrer *et al.* (2006) detects atmospheric blocking. The last column shows the 2-m maximum temperature anomalies with respect to a smoothed day-wise summer climatology, again for (c) June 1, 1982 and (f) September 18, 2018. [Colour figure can be viewed at wileyonlinelibrary.com]

depicted streamlines of the flow at 500 hPa (Figure 3a). This blocking is generally also easily identified by other blocking-detection algorithms. As an example, Figure 3b depicts, via hatching, the blocked grid points according to the algorithm of Scherrer *et al.* (2006), which is a 2D version of a 1D algorithm initially proposed by Tibaldi and Molteni (1990). In contrast to a case of full blocking, a recent case of a late Central European HW was initiated by a northward-extended subtropical ridge (Figure 3d). Such a flow anomaly is identified by the Sousa *et al.* (2021) algorithm, but would—by design—not be detected by blocking algorithms such as that of Scherrer *et al.* (2006) (see Figure 3e). However, in this example, the subtropical ridge-type HW leads to higher surface temperatures anomalies than the selected omega-blocking example (Figure 3c,f).

2.4 | Selection of archetypical omega- and ridge-type HWs

We now compile a list of HW cases featuring what we call archetypical cases of either omega blocking or the presence of a subtropical ridge. To do so, we compute for each of the 216 HWs the fraction of grid points within the Central European domain for which omega blocking or the presence of a subtropical ridge is identified by the algorithm of Sousa *et al.* (2021).

From the Sousa algorithm, we make use of the so-called instantaneous structure mask, which provides the blocking type per grid point regardless of whether it belongs to a persistent blocking object. Over the first four days of each heatwave, we then compute the temporal average of the relative fraction of grid points within the Central European domain identified as either instantaneous omega blocking or ridge presence. At the same time, we demand that, over the considered period of four days, the presence of other respective blocking types is low, with an average grid-point fraction of less than 10%. After exclusion of very weak HWs within the lower magnitude quartile and HWs with a duration of less than four days, we then select the 25 HWs with the highest respective relative area fraction of omega- or ridge-classified grid points. Upon further visual inspection of all cases selected, we replace a small number of cases in those samples that showed unusual flow evolution. These exchanges and the rationale behind them are documented in Figures S11 and S12 as well as Tables S2 and S3 in the Supporting Information. The choice of 25 cases each was found to be the best compromise between sample size and a clear distinction

between the large-scale flow evolution, not only during the respective HW onset but also throughout the following three days.

The final list of archetypical omega and ridge-type HW cases is presented in Table S1, along with some metrics of interest such as magnitude, duration, soil-moisture anomaly, and the average fraction of grid cells with either omega blocking or ridge presence. Although ridge-type HWs are slightly more intense, neither of the two samples is strongly skewed towards particularly long-lived or highly intense HWs. The corresponding large-scale circulation composite mean fields, as well as the respective time series of detected omega blocking or ridge presence, are displayed in Figure 4. The main features of the large-scale flow are seen quite distinctively in the composite mean and represent the archetypical picture of a subtropical ridge or an omega blocking well. The large-scale flow evolution for all individual 50 cases is presented in the Supporting Information (Figures S1–S10).

2.5 | Trajectory computation

To obtain quantitive information about the relative importance of different processes leading to anomalously high temperatures, we use a Lagrangian approach, utilizing ERA5 data at the full native spatial resolution of about 31 km with all available 137 vertical model

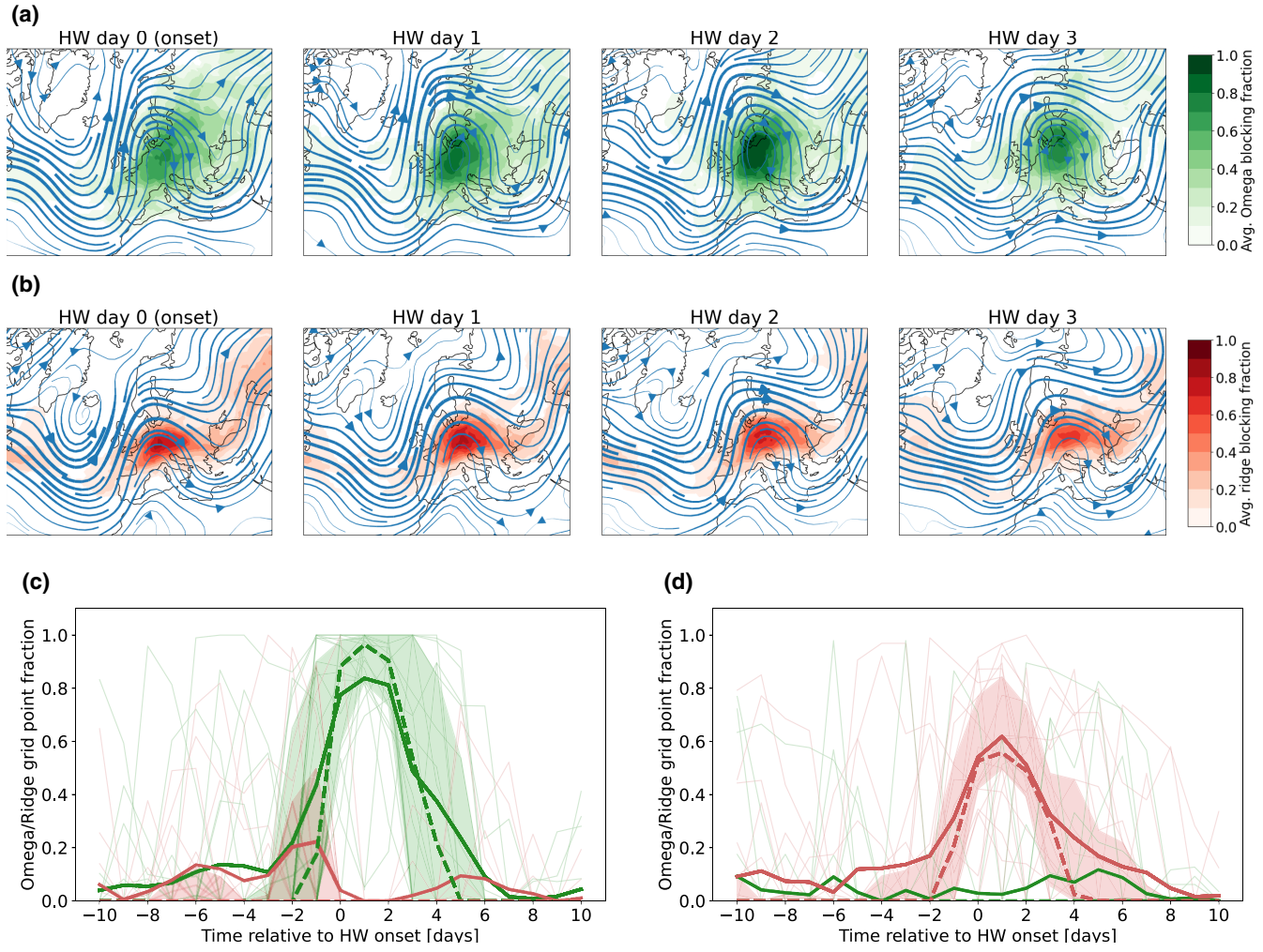

FIGURE 4 Composite mean circulation for the selected sample of the 25 most archetypical cases of HWs associated with either (a) an omega blocking or (b) the presence of a subtropical ridge. From HW onset to HW day 3, the composite-mean large-scale flow is shown in the form of streamlines based on 500-hPa daily mean winds. Coloured shading depicts the composite-mean relative occurrence of subtropical ridge detection (red) or omega blocking (green). The time series at the bottom depict the time series of detected omega blocking and subtropical ridge presence for (c) all 25 omega-type HWs and (d) all 25 ridge-type HWs. Omega (green lines) and ridge presence (red lines) are illustrated by the relative fraction of grid points in the Central Europe domain for which the algorithm has detected the respective feature. The arithmetic means are depicted as solid lines, whereas the median value is presented via dashed lines. Shadings show the respective interquartile range. [Colour figure can be viewed at wileyonlinelibrary.com]

levels. Using Lagranto (Sprenger & Wernli, 2015), we compute backward trajectories starting from the HW region over Central Europe. In contrast to Röthlisberger and Papritz (2023), we limit the backward integration to 10 days instead of 15 days. In our view, the saved computational cost outweighs the possibly limited added value, given that trajectories become increasingly sensitive to minimal changes in the starting position for longer integration times. To exclude regions close to the coastlines and higher orography, we have narrowed the initiation domain to a box spanning 7°E–13°E and 49°N–53°N (grey shading in Figure 2a).

Trajectories are started at every ERA5 grid point, that is, at about every 0.25° for two different sets of vertical levels. First, to analyse processes important for near-surface temperature anomalies, we start trajectories at the levels 10, 30, and 50 hPa above ground level. These are exactly the same vertical levels as used in Röthlisberger and Papritz (2023). Secondly, the levels 175, 200, and 225 hPa above ground level are chosen to characterize Lagrangian properties of air masses which are affected much less or not all by planetary boundary layer (PBL) processes. This choice is therefore somewhat analogous to the use of 850-hPa temperature in synoptic meteorology. For the sake of simplicity, we refer to this set of vertical starting positions as "top of PBL". The choice of fixed initiation levels facilitates the comparison with earlier studies looking at the vertical structure of HWs (e.g Hotz *et al.*, 2024) and compromises only slightly the idea of filtering out PBL processes. Even at 1500 UTC, during the peak of the diurnal boundary-layer development, on average more than 85% of trajectories are initiated above the local boundary height as provided by ERA5 (not shown).

Taking into account both the number of geographical starting positions and the respective three vertical levels each, we start about 1750 trajectories per initiation time step. Trajectories are first initiated for the HW onset day as provided by the objective HW detection algorithm. We refer to this day as HW day 0, as it is usually characterized by substantially lower spatially averaged temperature anomalies compared with later days. We then start trajectories every three hours until the end of HW day 3. Many of the selected HWs are not longer than four days in total, which is why the analysis will not extend beyond HW day 3.

2.6 | Lagrangian temperature anomaly decomposition

To each single trajectory, we apply the algorithm of Röthlisberger and Papritz (2023), which allows a decomposition of Lagrangian temperature anomalies into multiple terms, from which three of the most important can be readily interpreted as the temperature anomalies due to advection, adiabatic warming, and diabatic heating. Their algorithm is based on an equation for the material change of T', where T' is the Lagrangian temperature anomaly of an air parcel with respect to the climatological temperature $\overline{T}$ at the grid point and pressure level the air parcel is currently located at. For a given trajectory initiation time t_s at a given location x, the Lagrangian temperature anomaly decomposition for any traced air parcel T'(x, t_s) can then be obtained by integrating (in reverse temporal order) the following equation from the point in time at which T' was zero for the last time, called the anomaly genesis time t_g, until t_s:

$$
\begin{aligned}
T'(x,t_s) = &- \int_{t_g}^{t_s} \frac{\partial \overline{T}}{\partial t}\, d\tau - \int_{t_g}^{t_s} \mathbf{v}\cdot\nabla_h \overline{T}\, d\tau \\
&+ \int_{t_g}^{t_s} \left[\frac{\kappa\, T}{p} - \frac{\partial \overline{T}}{\partial p}\right] \omega\, d\tau \\
&+ \int_{t_g}^{t_s} \left(\frac{p}{p_0}\right)^{\kappa} \frac{D\theta}{Dt}\, d\tau + T'_{t=t_g},
\end{aligned}
$$

where $\overline{T}$ denotes the climatological temperature at a given grid point for a given day of the year and hour of the day. It is computed by averaging each three-hourly time step of the climatological period over a running 21-day window as well as over a 10-year window. Thereby, any dependence on seasonality or time of day is removed and climatological trends are also eliminated to a large extent. All other variables correspond to the usual meteorological notation. In the differential, τ is used instead of t to clarify that the integration uses discrete three-hourly time steps.

In the above equation, the first term refers to a seasonality effect that might have to be considered for individual HWs. In our case, where averages over many HWs from different parts of the summer season are calculated, it is close to zero and can therefore be neglected. The second term is referred to as temperature anomaly due to advection. More precisely, this term quantifies how T' is affected by the advection of the traced air parcel across horizontal gradients of the climatological temperature $\overline{T}$. The third term combines the effect of adiabatic compression as well as the vertical advection of the climatological temperature. Henceforth, we will refer to this as the temperature anomaly due to adiabatic warming. The fourth term quantifies changes in the potential temperature of the traced air parcel and can therefore be understood as the temperature anomaly due to any diabatic heating from radiation, surface sensible heat fluxes, or turbulent mixing. The last term is a residual that represents the initial temperature anomaly during genesis when the temperature anomaly flips to positive. In most cases this

residual is below 0.5 K, but it can be larger in the case in which the parcel's temperature anomaly remains positive during the entire 10-day backward integration (anomaly age > 10 days).

After the computation for each single trajectory, we postprocess the heating contributions and other Lagrangian characteristics of interest such as air-mass origin in the following way. First, we focus on the top 25% warmest air parcels for each initiation time step. For this, we compute the 75th spatial percentile of the air-parcel temperature anomaly at the given initiation height and given initiation time step and disregard all trajectories with air-parcel temperature anomalies below this threshold. For each HW day, the temperature anomaly decomposition and other Lagrangian characteristics of the 25% warmest tracked air parcels are then averaged over all eight initiation time steps per day. Moreover, we not only consider the heating decomposition for the last integration time step (i.e., the initiation time step of the trajectory) but also include the backward integration time steps −3, −6, −9, and −12 h. Finally, we average all anomaly decomposition terms further over the respective three initiation levels. The application of both temporal averaging methods—vertical averaging as well as averaging over the entire 25% of trajectories with the highest initial temperature anomaly—leads to a considerable reduction of noise in the data, as well as to an elimination of the effect of the diurnal cycle.

A key quantity of interest in this study is the relative roles of advection, adiabatic warming, and diabatic heating. These relative contributions are computed for each time step and each trajectory individually and averaged only afterwards. To compute them, we divide the respective absolute term by the sum of the absolute contributions of the three processes considered, and not the total temperature anomaly. In most cases, the sum of these three processes is nearly indistinguishable from the total anomaly. Moreover, to avoid small divisors in cases of compensating terms, the relative fractions are only computed when the sum of all three contributions exceeds 2 K (which is almost always the case, due to the focus on the 25% warmest grid points).

3 | LAGRANGIAN ANALYSIS OF HEAT-INDUCING PROCESSES FOR TOP-OF-PBL AIR PARCELS

In this section, we will now assess whether the processes leading to heat might differ fundamentally between HWs forming under an omega blocking and those that are initiated by a subtropical ridge. We start with the analysis of air masses initiated at levels of 175, 200, and 225 hPa above ground, which we refer to as top-of-PBL air masses. At this starting level, the role of boundary-layer effects and night and day fluctuations is greatly reduced, which usually provides a clearer picture of the air-mass characteristics.

Figure 5 provides an overview over the pathway of air masses towards the Central European HW region, for both the respective HW onset day (top) and HW day 3 (bottom). Note that we only trace air parcels that were initiated over the 25% warmest grid points at a given time over the Central European HW region. The air masses that are eventually hovering over the HW region over Europe do usually originate from the Atlantic ocean, during both the onset and the mature HW stage (Figure 5a,h). In ridge-type HWs, the air masses mostly take a more southern route, particularly in the more mature phase of the HW, where air parcels often traverse the Iberian peninsula before arrival in Central Europe. In the omega composite, air masses generally have a slightly more northerly origin over the Atlantic. Especially towards the mature HW phase, they also move in a distinctive anticyclonic fashion around the omega anticyclone to flow into the HW region from a northeasterly direction. These two main inferences about air-mass origin and the average pathway not only apply for the average over all 25 cases (thick lines) but are also mostly true for all individual HW cases (thin lines).

Moreover, we find that air masses originate from similar pressure levels with a mean of 600–650 hPa at 10 days of backward integration. However, omega-related air masses stay at higher altitudes until 48 h before arrival, after which they finally descend more rapidly than air masses associated with the ridge sample (Figure S13 in the Supporting Information).

We explore further the location and point in time at which air parcels first become anomalously warm with respect to a background climatology at the current location and altitude of the air mass. As in Röthlisberger and Papritz (2023), this is called anomaly genesis time and location and is marked via green hexagons for the omega cases and red triangles for the ridge cases. During the HW onset phase, air masses reaching the HW area region have in many cases become anomalously warm over the Atlantic, some 2000–3000 km west of the Central European focus region. The height at which the anomaly genesis takes place varies considerably between 550 and 850 hPa, with, on average, consistently slightly higher genesis altitudes in omega-type HWs, but no statistically significant differences (Figure 5e). The latitude and longitude at which the air masses first become anomalously warm do not differ in a statistically significant way between ridge- and omega-type HWs (Figure 5c,d). The same applies to the anomaly age (time between anomaly genesis and arrival at HW region) and the anomaly formation distance (Figure 5f,g). During the mature phase of the HW, the

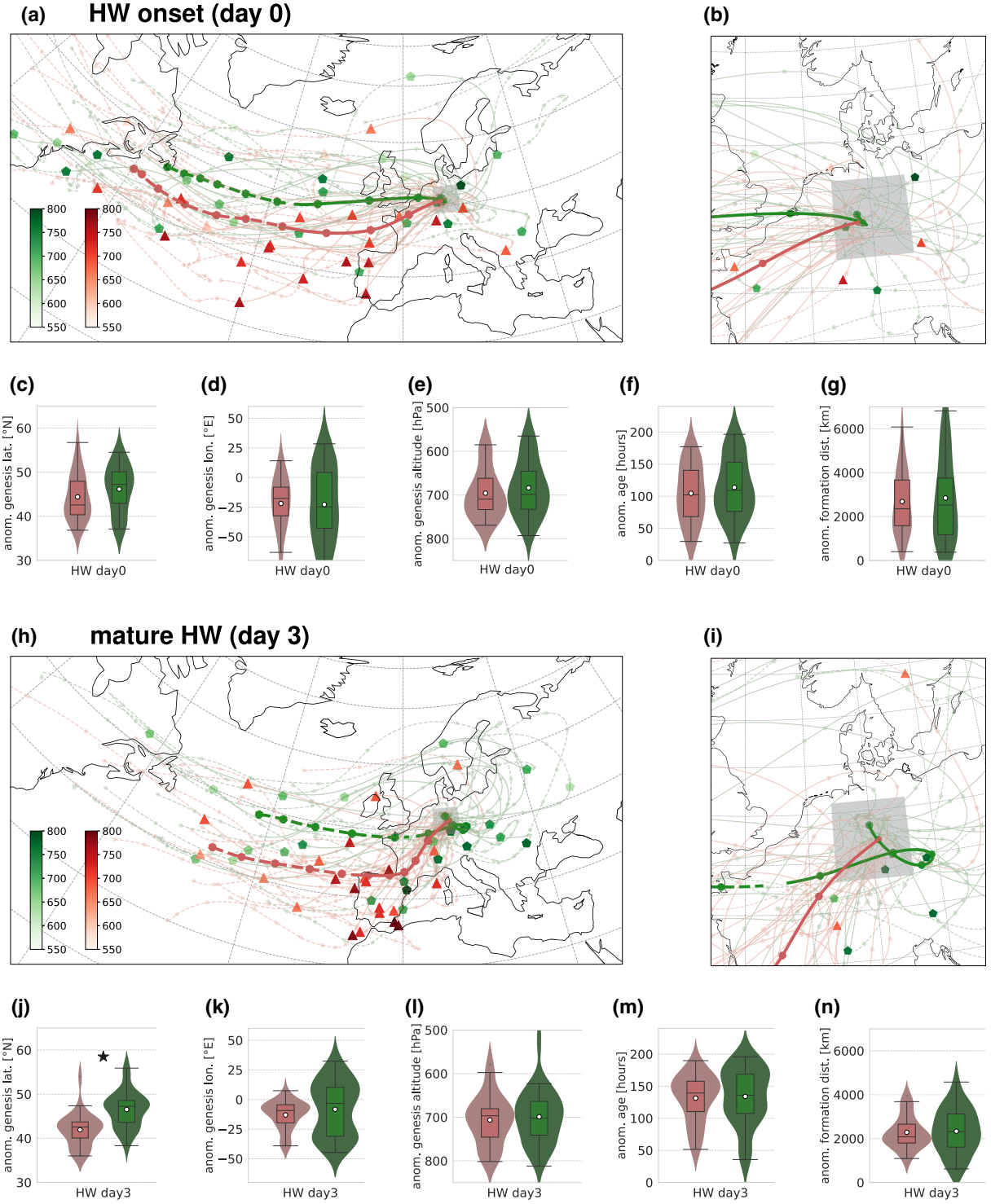

FIGURE 5 Comparison of top-of-PBL air-mass origin and pathway between ridge-type (red colours) and omega-type (green colours) HWs for the onset phase (HW day 0) and the more mature stage (HW day 3). The maps in (a, h) and the zoom-in in (b, i) show, for each HW case, average 10-day backward trajectories started over the Central European domain of interest at the levels 175–225 hPa above ground (thin lines). Small dots along the paths denote backward trajectory integration at an interval of 24 hours. Green/red circle/triangle markers denote the so-called average anomaly genesis location and the respective red and green colour bars indicate the pressure level of anomaly genesis. The two thick lines show the air-mass path averaged over all 25 ridge or omega-type HW cases, respectively. Lines are printed with a dashed pattern when the air mass is not yet anomalously warm. Box plots show the statistical distribution of HW-case averaged anomaly genesis (c, i) latitude, (d, j) longitude, (e, l) altitude, and (f, m) age of the anomaly, as well as (g, n) formation distance. A black asterisk denotes statistical significance in the difference of means at the 5% level, as evaluated via bootstrapping with 10,000 iterations. [Colour figure can be viewed at wileyonlinelibrary.com]

majority of cases feature an anomaly genesis closer to or directly over the European continent and we observe a more distinct separation between omega and ridge cases. For ridge-type HWs, in about 50% of the cases air masses first become anomalously warm over or near Iberia at a pressure level between 750 and 850 hPa. In contrast, anomaly genesis regions vary more for omega-type HWs, with one cluster being close to the HW region, whereas in some cases anomaly genesis takes place quite far away over the Atlantic. Despite the quite high case-to-case variability, we find a statistically significant difference for the genesis latitude (Figure 5j), with omega-type HWs featuring an average of 46.5°N and ridge-type HWs showing an average of around 42°N. However, the genesis longitude and altitude, as well as the genesis age and formation distance, show no statistically significant differences during the mature HW phase (Figure 5k–n).

HW days 1 and 2 do not show unexpected behaviour, but mostly a gradual transition from the situation described during HW onset to the characteristics of the mature HW stage. As on HW day 3, significant differences are found in the anomaly genesis latitude on HW days 1 and 2, with ridge-type HWs featuring a more southerly air-mass origin (Figure S14).

Figure 6a provides an overview of the average air-parcel temperature anomaly of all trajectories that started from the 25% warmest grid points at the levels 175, 200, and 225 hPa above ground. During HW onset (day 0), on average air parcels at the top of the PBL are 6 K warmer than the climatology for both ridge- and omega-type HWs.

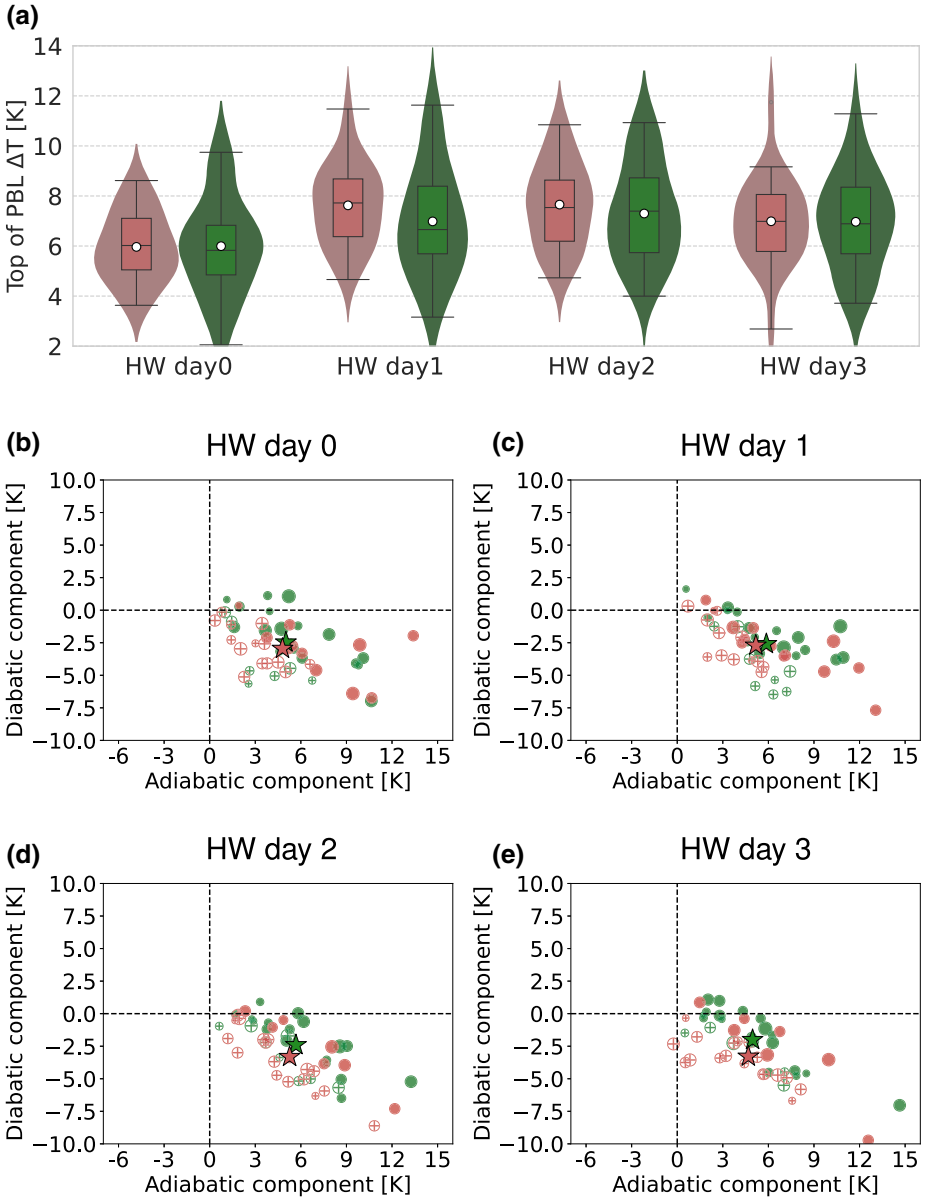

FIGURE 6 Comparison of top-of-PBL air temperature anomalies and Lagrangian temperature decomposition between 25 ridge-type (red colours) and 25 omega-type HWs (green colours). The box plots in (a) show, separately for each HW day considered, the air-parcel temperature anomaly of the 25% warmest grid points within the CE domain, averaged over all eight initiation time steps per day and also averaged over four backward trajectory integration time steps. Correspondingly, the scatter plots (b–e) depict the Lagrangian decomposition of these temperature anomalies according to the algorithm of Röthlisberger and Papritz (2023). For each heatwave, each circle presents the contribution of the diabatic and adiabatic components. A strong relative contribution by advection (more than a third of the total temperature anomaly) is denoted by a cross-hair symbol. Coloured star symbols represent the centroid of the respective distributions. The size of the circles scales with the respective HW intensity. [Colour figure can be viewed at wileyonlinelibrary.com]

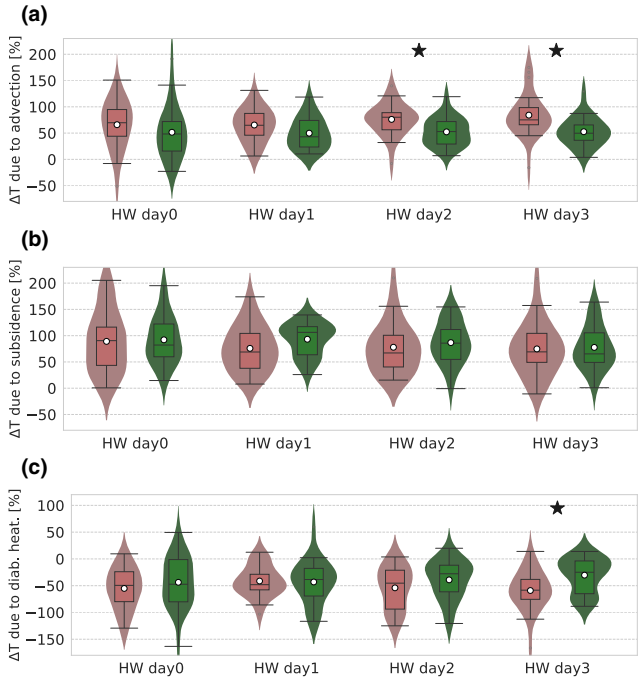

FIGURE 7 Comparison of relative contributions of (a) advection, (b) adiabatic warming, and (c) diabatic heating for top-of-PBL air masses between 25 ridge-type and 25 omega-type HWs. The box plots show, corresponding to the absolute contributions shown in Figure 5, the relative contributions of the three processes as diagnosed by the Lagrangian temperature algorithm of Röthlisberger and Papritz (2023). Please note the use of a different *y*-axis in (c). Stars at the top of the box plots denote a statistically significant difference in the mean between ridge-type and omega-type HWs at the 5% level, tested by bootstrapping with 10,000 iterations. [Colour figure can be viewed at wileyonlinelibrary.com]

On day 1, the 25 selected ridge-type HWs feature slightly higher anomalies of nearly 8 K on average, whereas the average anomaly for the 25 omega-type HWs amounts to about 7 K. Similar anomalies exist on HW day 2. On the final HW day considered, day 3, omega-type and ridge-type HWs again exhibit nearly equal anomalies of about 7 K. None of the air-mass temperature differences are statistically significant.

The Lagrangian temperature anomaly decomposition is shown in the scatter plots in Figure 6b–e in absolute terms and for all individual cases. The relative contributions to the temperature anomaly are shown in the form of box plots in Figure 7. At the top of the PBL, the largest contribution to anomalous temperatures is the adiabatic warming due to subsidence (Figure 7b). For all HW days, and particularly on day 1, omega-type HWs show a higher percentage, but the differences from ridge-type HWs are not statistically significant on any HW day. Despite the high case-to-case variability among the respective samples (Figure 6d,e), significant differences are found in the effect of advection for the more mature phase of HWs on days 2 and 3 (Figure 7a). As might be expected, ridge-type HWs show a substantially higher contribution due to advection. In the Lagrangian sense that means that the air masses reaching the HW region have crossed more isotherms of climatological temperature or, more simply, they have come from climatologically warmer regions. Consistent with the anticipated characteristics of air masses that are mostly above the PBL, diabatic processes show a negative contribution to the temperature anomaly (Figure 7c). In other words, the air parcels reaching the HW region will likely have cooled by radiation, but the temperature change due to adiabatic compression will often be greater than that because of radiative cooling.

As mentioned in Section 2, a small part of the actual temperature anomaly cannot be accounted for, particularly when the air parcel has been uninterruptedly anomalously warm for more than 10 days. For all HW days, we find that this residual remains below 1 K with median values of around 0.7 K. Only on HW day 3 is there a significant difference, with omega-type HWs featuring a residual of 0.93 K compared with 0.67 K for ridge-type HWs (not shown).

The statistical differences between omega- and ridge-type HWs are not sensitive against the exact number of trajectories included in the analysis, as long as we focus on including enough trajectories with a reasonably high temperature anomaly. The average relative contributions to the anomalously high temperatures do not change substantially when we use 33% or only the top 10% of warmest grid points (not shown). Moreover, the trajectory initiation level does not affect our main results substantially. Irrespective of whether we only include trajectories started at either 175 hPa or 225 hPa above ground, we again find a significantly higher contribution of advection in ridge-type HWs on day 2 and 3 (not shown).

In Section 2, we reported on the manual replacement of some cases with flow configurations not deemed to be archetypical. This decision has no impact on the robustness of our findings. On the contrary, the samples of 22 objectively identified ridge-type and 25 omega-type HWs even show slightly more pronounced differences in each of the heat-generating mechanisms (Figure S15 in the Supporting information).

4 | LAGRANGIAN ANALYSIS OF HEAT-INDUCING PROCESSES FOR NEAR-SURFACE AIR PARCELS

Compared with top-of-PBL air masses, the origin and pathway of air masses reaching the HW area near the surface

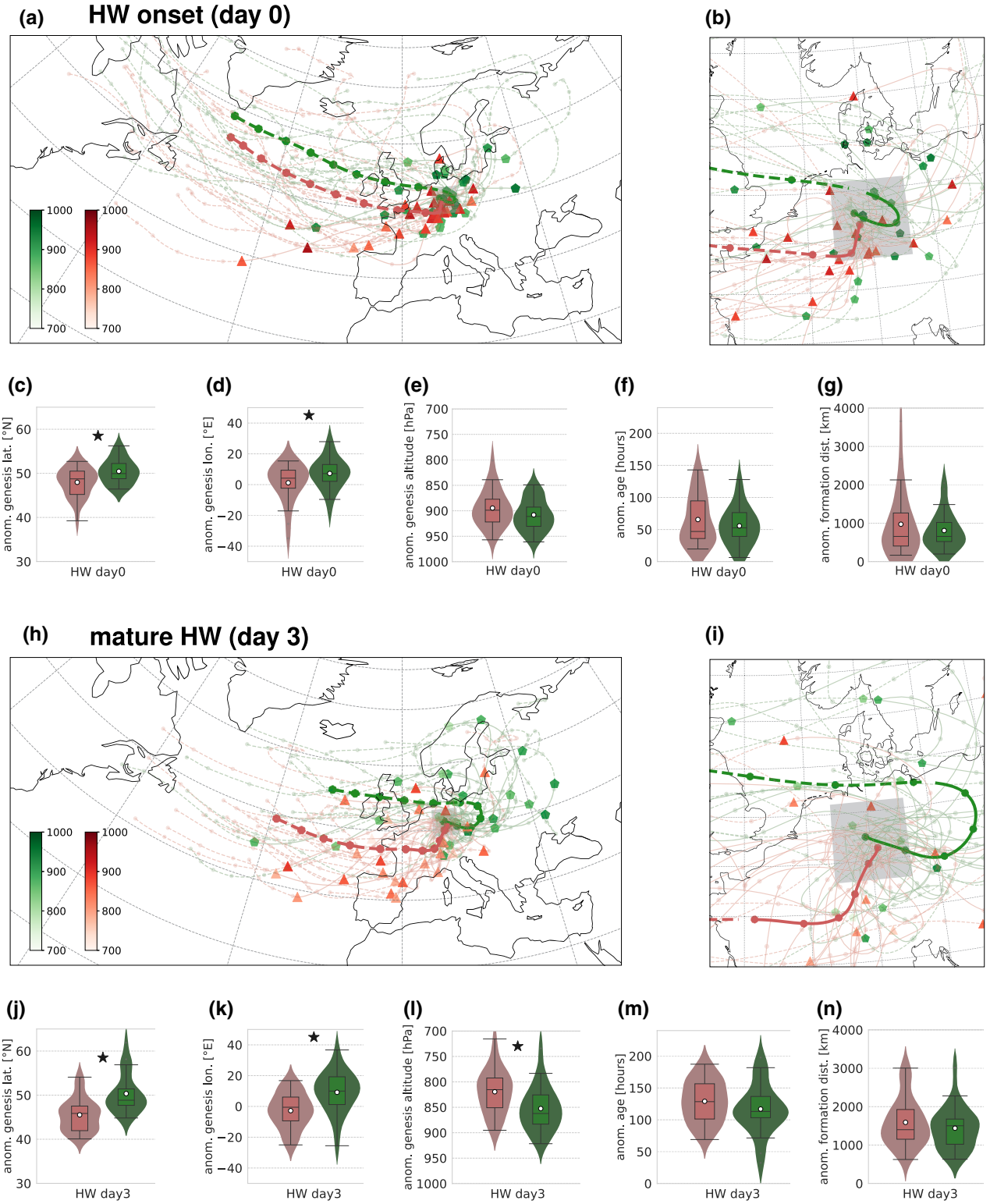

FIGURE 8 Same as Figure 5, but for trajectories started near the surface (10, 30, and 50 hPa above ground level). [Colour figure can be viewed at wileyonlinelibrary.com]

are in general slightly shifted to the north (Figure 8a,b). During the HW onset phase, differences in the geographical origin of HW-related near-surface air masses appear rather small. However, significant differences are present in the average anomaly genesis location. Air masses associated with ridge-type HWs become anomalously warm further south (48°N versus 50.5°N) and further west (1°E versus 7°E) compared with omega-type HWs

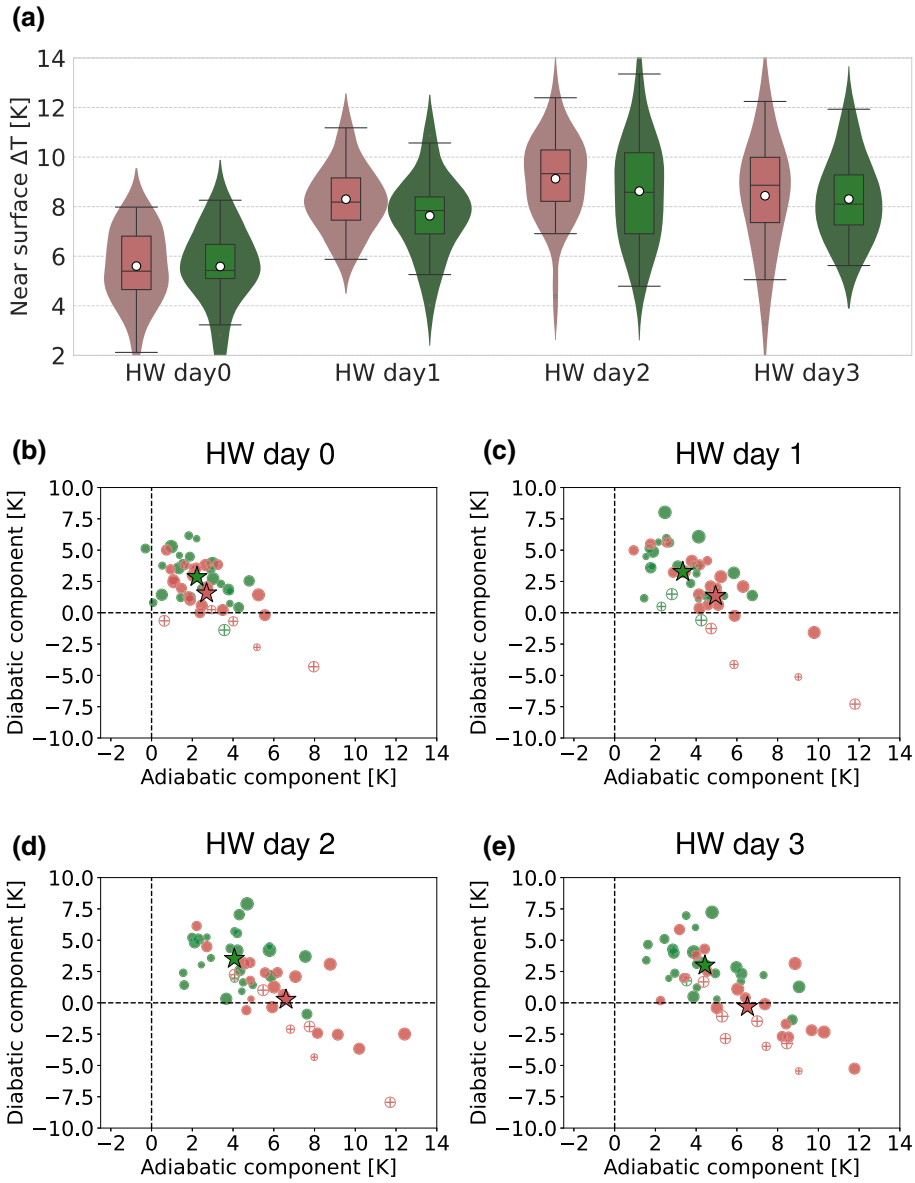

FIGURE 9 Same as Figure 6, but for trajectories started near the surface (10, 30, and 50 hPa above ground level). [Colour figure can be viewed at wileyonlinelibrary.com]

(Figure 8c,d). In comparison with the case of top-of-PBL air masses discussed previously, anomaly genesis is therefore closer to the HW region (median genesis formation distance < 1000 km, see Figure 8g). Consequently, the air masses have only been anomalously warm for about 2 days prior to arrival, with no substantial differences between the omega- and ridge-type HWs (Figure 8f).

During the mature phase of the HW, air masses reaching the HW region near the surface have not travelled as great a distance over 10 days compared with the onset phase (Figure 8h,i). However, this does not imply that the anomaly formation also takes place closer to the HW area. In fact, the opposite is true on average, with genesis formation distance increasing by about 30% (Figure 8m). This is directly related to the time of anomaly formation. When air masses reach the HW area, they have on average already been anomalously warm for about 4–5 days, which is more than twice as long as during the onset phase. Similar to the top-of-PBL air masses, the differences in the origin and pathway of air masses between ridge- and omega-type HWs become more apparent during the mature HW stage. In a majority of omega-type cases, air parcels reach the HW region from a northeasterly direction after travelling in an anticyclonic manner around the omega block. In the ridge sample, this is only observed for one outlier case, while all other cases show air masses approaching from westerly and southwesterly directions. Regarding the anomaly genesis, we also identify statistically significant differences in both longitude and latitude (Figure 8j,k). In ridge-type HWs, a sizeable cluster is found in the vicinity of Iberia, while in some other cases the genesis is closer to the HW region but generally to the southwest of it. In contrast, omega HWs often exhibit anomaly genesis locations north of the HW area, with

considerable inter-case variability, involving genesis locations over the Atlantic, Scandinavia, and also Northwest Russia.

The average movement of air masses in the vertical plane shows only minor differences between omega- and ridge-type HWs. Overall, air masses reaching the surface tend to originate from altitudes around 700 hPa on average, with negligible differences between both samples (Figure S16). An exception is the onset phase, for which ridge-type HW air masses tend to come from initially slightly higher altitudes (~ 20 hPa), which leads to a slightly faster descent over the course of the final two days until arrival in the HW region. When it comes to the altitude at which air masses first become anomalously warm, which is on average found to be between 850 and 800 hPa, we do find that the anomaly genesis altitude in ridge-type HWs is consistently higher during all HW phases (Figure 8e,l). While the difference is not significant during HW onset, it has already become statistically significant at the 5% level on HW day 1 (Figure S17 in the Supporting Information).

As was the case for top-of-PBL air masses, we see a rather smooth transition in the air-mass origin characteristics between onset and HW day 3. The genesis latitude on HW day 1 and both the genesis longitude and latitude on HW day 2 exhibit significant differences, with omega-type HWs featuring more northerly and easterly anomaly genesis locations, consistent with the anticyclonic pathway (Figure S17).

Besides overall slightly higher anomalies, the evolution of near-surface anomalies from onset to day 3 is very similar to the anomalies at the top of the PBL discussed earlier. Moreover, there are again no statistically significant temperature anomaly differences between ridge and omega cases (Figure 9a). During HW onset (day 0), the temperature of near-surface air parcels is increased by about 6 K with respect to the running summer climatology. On days 1 and 2, the 25 selected ridge-type HWs feature slightly higher average anomalies of up to 9 K, while the 25 omega-type HWs exhibit temperature anomalies of up to 8.5 K. In a slight contrast to top-of-PBL air, ridge-type HWs also keep being slightly warmer than omega HWs on the final HW day considered.

Near the surface, the role of advection is overall weaker compared with air masses at the top of the PBL. However, ridge-type HWs still consistently feature an average relative contribution of about 15% throughout all HW days, while the role of advection is on average close to zero in omega-type HWs (Figure 10a). This means that in omega-type HWs the air masses usually originate from regions that feature climatological temperatures similar to the Central European focus region.

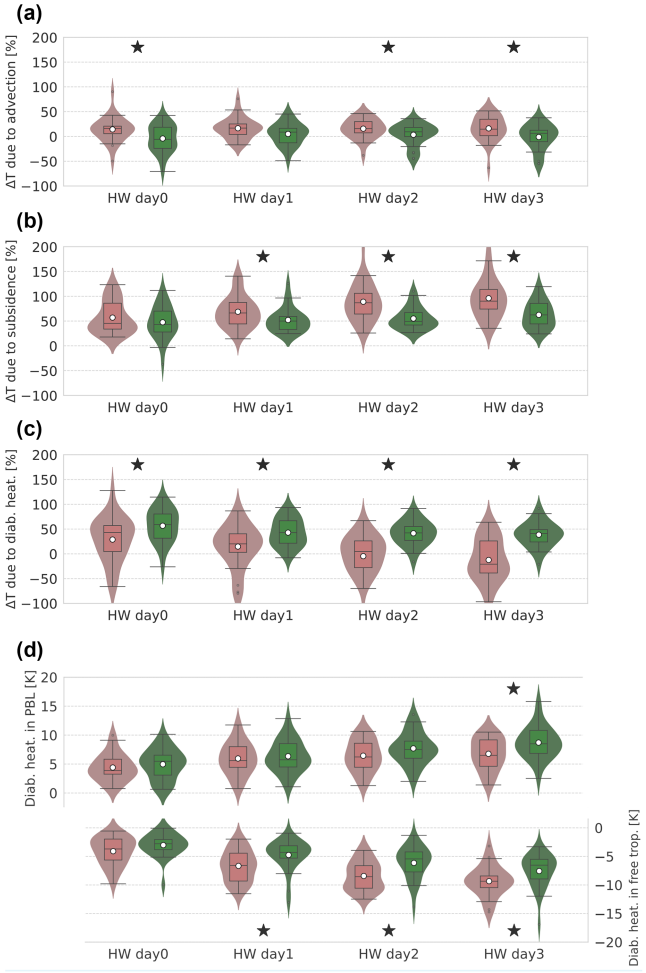

FIGURE 10 (a–c) Same as Figure 7, but for trajectories started near the surface (10, 30, and 50 hPa above ground level). Panel (d) adds a decomposition of the diabatic heating integrated along trajectories into the respective contributions from the time within the PBL (heating; upper box plots) and the time at which air masses were still in the free troposphere (mostly cooling; lower box plots). [Colour figure can be viewed at wileyonlinelibrary.com]

In contrast to the air masses at the top of the PBL, we now detect statistically significant differences in the role of subsidence for the more mature phase of the HW. During the onset, both ridge-type and omega-type HWs exhibit relative contributions from adiabatic warming of around 50% (Figure 10b). On HW day 2 and HW day 3, this fraction stays roughly the same for omega HWs, while the relative contributions rise sharply to nearly 100% for ridge-type HWs, leading to a clearly statistically significant difference at the 5% level. The differences in the adiabatic warming fraction are consistent with the higher anomaly genesis altitude for ridge-type HWs, which allows for more adiabatic compression, although the vertical gradient in climatological temperature along the respective air-mass paths also has to be taken into account.

For near-surface air parcels, diabatic heating is now an important process. Particularly during HW onset, nearly all 50 HW cases considered feature positive diabatic contributions to the overall temperature anomaly (Figure 10c), with only a few outliers, mainly among the ridge-type HWs (Figure 9b,c). The overall positive contribution is expected, as air parcels near the surface will be exposed to warming due to sensible heat fluxes and turbulent mixing whereas air masses outside the PBL will mostly just experience radiative cooling. There are significant differences in the relative importance of diabatic warming between ridge- and omega-type HWs. From onset to HW day 3, omega-type HWs always feature a higher diabatic contribution on average. On days 2 and 3, when ridge-type HWs no longer feature a substantial diabatic contribution, these differences are statistically significant. During the mature HW phase, omega-type HWs still exhibit diabatic contributions of around 40%. However, compared with the onset phase, this is also lower by some 20%. The apparent differences in the sample means are also reflected well by the frequency of cases for which diabatic heating no longer contributes positively. While this the case for only one omega-type HW on HW days 2 and 3, about a third of the 25 ridge-type HWs feature diabatic cooling during the mature HW phase (Figure 9d,e).

The observation that the relative importance of diabatic processes diminishes slowly over the course of the four HW days considered is not unexpected. During the onset of a heatwave, the surface might heat up nearly instantaneously in a typical high-insolation situation, whereas the near-surface air mass usually warms gradually over one or two days. As such, the sensible heat flux from the surface is expected to decrease and consequently lower the role of diabatic processes over the course of the HWs. The same argument may also explain the significant differences between ridge- and omega-type HWs. Either when an already warm air mass is transported horizontally to the HW region or when the air mass is warmed substantially by adiabatic compression, sensible heat fluxes will be lower due to the decreased difference between the radiatively heated surface and the overlying air mass. Hence, in ridge-type HWs with a stronger role of advection and subsidence, diabatic heating will play a less important role or there might even be net diabatic cooling.

As was the case for air masses initiated higher up, the residual term of the Lagrangian temperature decomposition remains well below 1 K on all HW days and there are also no significant differences between omega- and ridge-type HWs (not shown). Moreover, the main inferences for the near-surface case are again insensitive towards the exact choice of trajectories included with respect to the temperature anomaly (not shown). The significant differences between ridge- and omega-type HWs also remain mostly unchanged if we select just one single vertical initiation level instead of taking the average over 10, 30, and 50 hPa above ground. Closest to the surface, the advective component becomes on average close to zero for ridge cases and turns slightly negative for omega cases, but the differences remain significant (Figure S18). In turn, the diabatic component increases for both HW samples, while the adiabatic component stays mostly constant. Changes in the opposite direction are observed when only trajectories started from 50 hPa above ground are considered instead of the 10–50 hPa above ground mean (Figure S19). Such sensitivities are expected, as air masses are less and less affected by diabatic heating from surface sensible heat fluxes with increasing distance from the surface.

We have again tested the impact of the decision to replace HW cases with untypical flow evolution manually. Very similarly to the analysis of top-of-PBL air masses, the differences between 22 objectively identified ridge-type and 25 omega-type HWs turn out to be even slightly more distinct (Figure S20). This underlines that the robustness of the results presented here is not inflated by subjective decisions made during compilation of the respective HW samples.

Another important question is whether the role of heat-generating processes also shows significant differences with respect to the HW intensity. Within the sample of 50 selected HWs, we have therefore compiled two samples containing the 13 most intense and 13 least intense HWs irrespective of flow anomaly type. The differences in the respective relative fractions of advective, adiabatic, and diabatic components are clearly less distinguishable than for the comparison based on flow type (Figures S21, S22). Hence, the relative importance of the heat-generating processes might be associated more strongly with the type of atmospheric flow anomaly rather than the intensity of the heatwave itself.

5 | A DEEPER LOOK INTO THE ROLE OF DIABATIC PROCESSES

Now focusing exclusively on near-surface air masses, we elaborate on the key factors that set omega- and ridge-type HWs apart. The role of advection is straightforward to understand and needs no further investigation. Ridge-type HWs are on average characterized by the transport of air masses from more southern and therefore climatologically warmer regions. Similarly, we have seen that ridge-type HWs are characterized by anomaly genesis at higher altitudes, which is consistent with a significantly stronger role of adiabatic warming. More interesting is a closer look into the role of diabatic processes along the respective air-mass paths. Omega-type HWs exhibit a stronger role

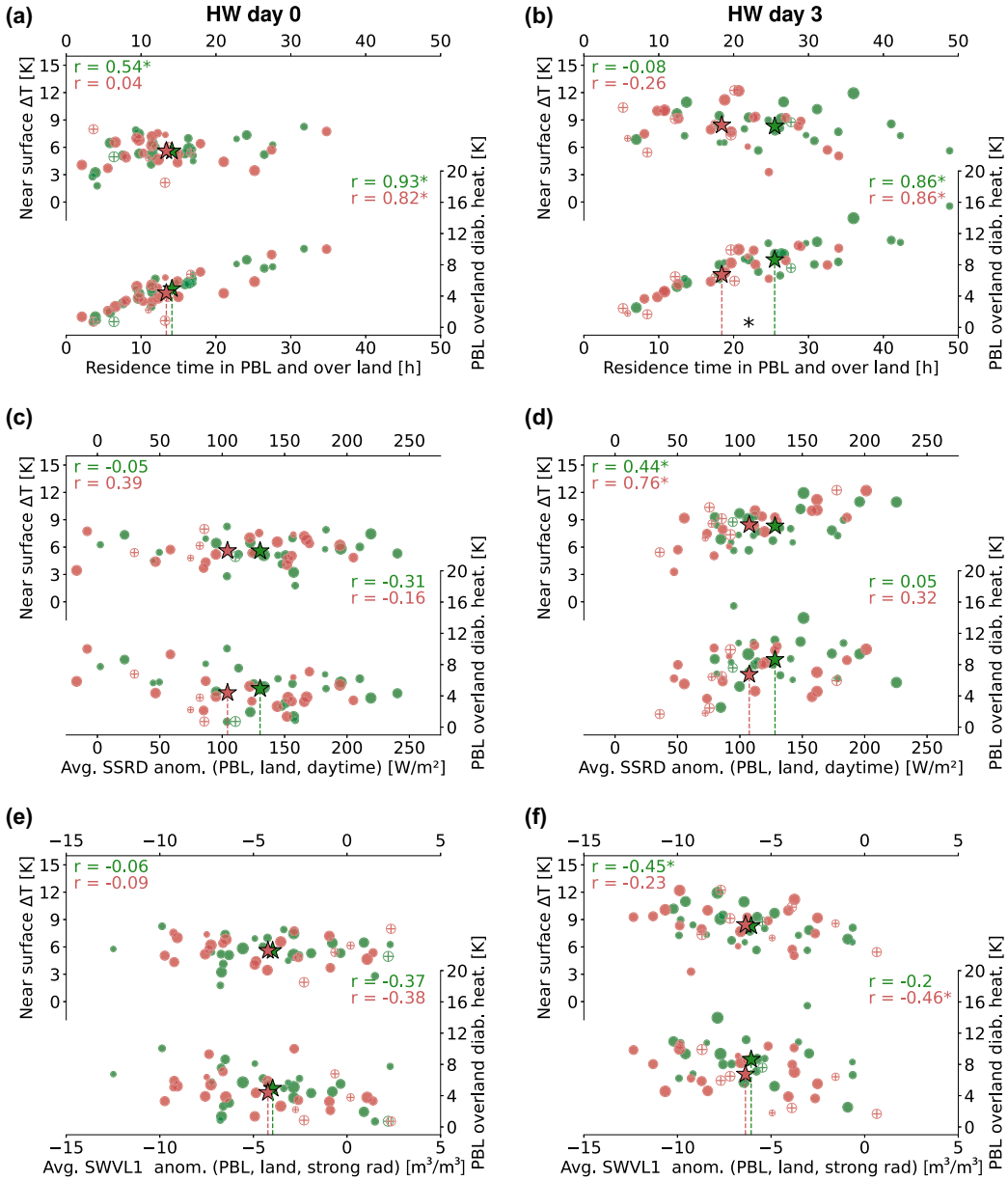

FIGURE 11 Investigation of the role of PBL processes for omega- and ridge-type HWs during onset (day 0) and the more mature stage (day 3) of ridge- and omega-type HWs. For each of the 50 HW cases selected, each data point represents the average over all trajectories started from the 25% warmest grid points at the initiation levels 10, 30, and 50 hPa above ground level. Each scatter plot displays both the near-surface air-parcel temperature anomalies and their diabatic component as a function of a selected quantity related to the diabatic heating of air masses close to the surface: (a,b) relative time fraction air parcels have on average spent in the PBL and over land simultaneously since anomaly genesis; (c,d) average anomalies in downward short-wave radiation (SSRD) along trajectory path (anomalous values are only considered when the air parcels are over land and in the PBL during daytime); (e,f) soil-moisture anomalies in the first soil layer (SWVL1), but only for times of strong radiation > 500 W/m^2. The statistical relationships between temperature anomalies and PBL quantities are quantified by Pearson's *r* for both ridge- (red font) and omega-type HWs (green font) separately (* denotes statistical significance at the 5% level). [Colour figure can be viewed at wileyonlinelibrary.com]

of diabatic heating compared with ridge-type HWs. For a deeper understanding, we have extended the algorithm of Röthlisberger and Papritz (2023) to estimate the time air parcels spend in the PBL. For this, we consider all time steps for which an air parcel is below 80% of the local ERA5-based PBL height and over land simultaneously. Similarly we also consider air parcels to be situated in the free troposphere if their altitude exceeds 120% of the local PBL height.

Surprisingly, a large fraction of the differences in the total diabatic heating between ridge- and omega-type HWs is attributable to significant differences in the integrated

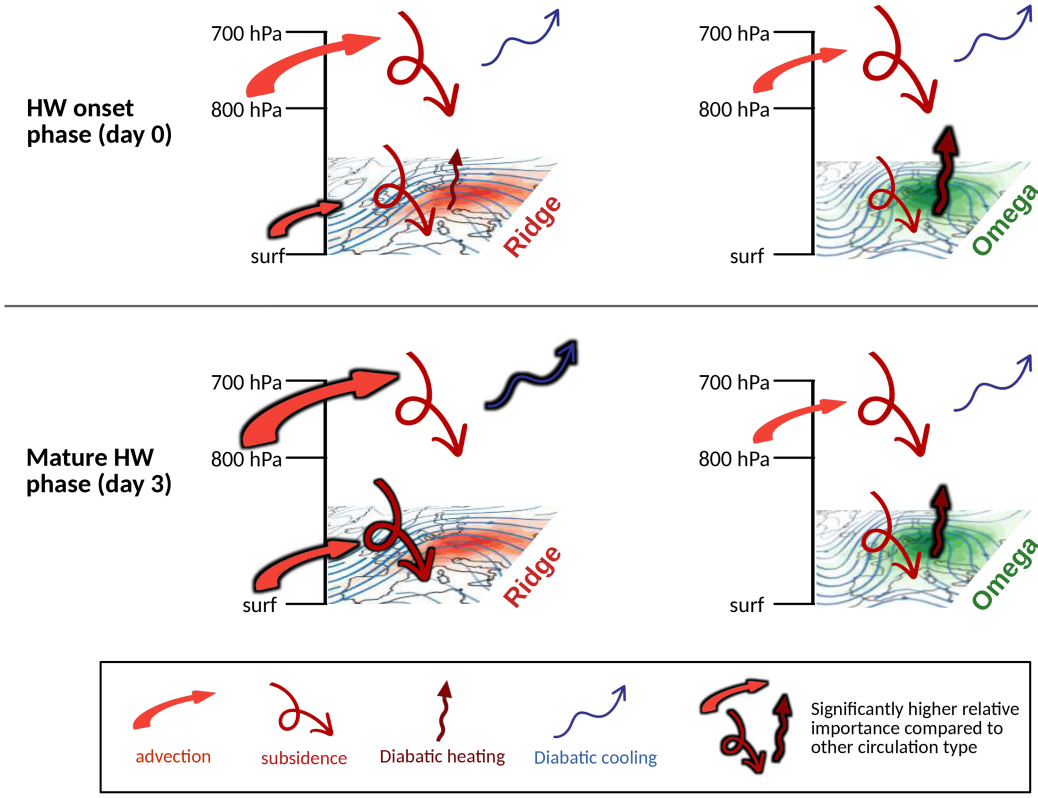

FIGURE 12 Schematic depiction of the key results of this study. The top row shows a comparison of the relative importance of the processes of advection, subsidence warming, and diabatic heating between ridge- and omega-type HWs for the onset phase (day 0). Correspondingly, the bottom row shows the same comparison but for the mature phase of the HW (day 3). The key findings are shown for both near-surface air masses and air masses at the top of the PBL. The relative sizes of the arrows depicting the respective processes represent their respective relative importance. If the average relative contribution is around zero, the respective arrow is omitted. A significantly higher relative importance with respect to the other circulation type is indicated by a shadow highlight around the respective arrow. Note that the total diabatic heating displayed here can also be understood as the sum of an earlier negative contribution from radiative cooling while air parcels are still in the free troposphere and a later contribution by heating from turbulent heat fluxes and mixing. [Colour figure can be viewed at wileyonlinelibrary.com]

diabatic cooling while air parcels are still in the free troposphere (Figure 10d, lower box plots). These differences have already become significant at HW day 1 and increase continuously to about 3 K on average until HW day 3. The stronger diabatic cooling in ridge-type HWs is likely related to both the slightly higher anomaly age (time between anomaly genesis and arrival at HW region; Figure 8m) and a slightly elevated genesis level for ridge-type HWs (Figure 8l), leaving more time for radiative cooling in the free troposphere compared with omega-type HWs. We do not find any robust evidence for a substantial role of condensation heating in either omega- or ridge-type HWs (not shown).

The significantly larger role of diabatic heating in omega-type HWs is increased further by differences in diabatic heating within the PBL. On HW day 3, this difference of about 2 K becomes statistically different at the 5% level (Figure 10d, upper box plots). The main reason for these differences is the amount of time spent in the PBL, which becomes consistently higher for omega-type than ridge-type HWs with each HW day. During the HW onset phase, air parcels reaching near-surface levels have on average spent little more than 12 hours in the PBL and over land, which is around a quarter of the time since anomaly genesis (Figure 11a). Towards the later stages, PBL residence time increases to around one day, with omega-type HWs spending about 6 hours longer in the PBL over land on average (Figure 11b, see Figure S23 for HW days 1 and 2). As expected, the amount of time spent in the PBL is strongly positively correlated with diabatic heating. However, this is not the case for the total temperature anomaly. On the contrary, during the mature HW phase, the residence time in the PBL is significantly negatively correlated with the total temperature anomaly for ridge-type HWs. Hence, the more intense HWs of the ridge type are linked to cases of rather fast descending air masses with little impact of diabatic heating in the PBL.

Total temperature anomalies as well as the diabatic component may ultimately be affected not only by the time spent in the PBL but also by anomalies in quantities affecting surface sensible heating. Therefore, we temporally integrate downward short-wave radiation along the trajectory paths for all daytime time instances, for which the air parcels are over land and within the PBL. Nearly all HWs analysed feature positive insolation anomalies along the trajectory pathways, ranging from −10 to 250 W/m^2. However, in contrast to the amount of time spent in the PBL, ridge- and omega-type HWs do not feature significant differences in the amount of short-wave radiation near-surface air masses are subjected to (Figure 11c,d). Moreover, the integrated short-wave radiation anomaly along trajectory paths is not significantly correlated with PBL diabatic heating.

Finally, we analyse the role of soil-moisture anomalies along the trajectory pathways. Desiccated soils strongly increase the ratio of sensible to latent heat fluxes, but a substantial effect on air-mass heating should only be expected during times of strong insolation. We therefore integrate soil-moisture anomalies for those time instances for which air parcels are within the PBL and also a strong insolation of more than 500 W/m^2 is present. We find that both omega- and ridge-type HWs are characterized by very similar negative soil-moisture anomalies along the trajectory paths. The average deficit increases from 4.5% to 7% from onset to HW day 3, but no significant differences exist between ridge- and omega-type HWs (Figure 11e,f). Similarly to short-wave radiation anomalies, we find no clear relationship between soil-moisture anomalies along air-mass paths and the amount of integrated diabatic heating. It should be noted that our analysis only focuses on the nearly immediate interaction of near-surface air masses with the uppermost soil layer along trajectory paths and is also limited by the rather small sample size. A different picture may arise when the relationship between soil moisture and omega blocking or ridge presence is analysed over longer time scales.

6 | SUMMARY AND CONCLUDING DISCUSSION

In Central Europe, heatwaves (HWs) can typically be enabled by the presence of an omega blocking, but also by poleward ridging of the subtropical high-pressure belt. Moreover, anomalously high temperatures in European HWs are attributable to positive contributions from the three processes of advection, adiabatic warming, and diabatic heating. Most previous studies assign particular importance to the latter two processes, but stress regional differences and a high case-to-case variability (Bieli *et al.*, 2015; Röthlisberger & Papritz, 2023; Sousa *et al.*, 2020; Zschenderlein *et al.*, 2019). We therefore hypothesized that the relative importance of the three heat-generating processes may be linked to the respective large-scale atmospheric flow during HW formation.

Based on an objective blocking identification algorithm by Sousa *et al.* (2021), we therefore selected 25 archetypical cases of HWs associated with a classic omega blocking and 25 cases linked to subtropical ridges during the period 1950–2023. For each HW day from the onset (day 0) to HW day 3, we computed ERA5-based backward trajectories that were initiated either near the surface or around the top of the PBL over the Central European HW area. Finally, we adopted the Lagrangian temperature anomaly decomposition technique from Röthlisberger and Papritz (2023) to find the following answers to our research questions.

- *Where do air masses involved in Central European HWs usually come from and are there substantial differences between HWs associated with an omega blocking and those initiated by subtropical ridges?*

  At the top of the PBL (175–225 hPa above ground), air masses involved in Central European HWs originate mostly from westerly and southwesterly directions during the onset phase, but with considerable case-to-case variability. Towards the more mature stage, distinct differences emerge between ridge- and omega-type HWs, with a statistically significant more southerly origin of air masses for ridge-type HWs. HWs associated with subtropical ridges are characterized by a transport of air masses from southwesterly regions, with air masses first becoming anomalously warm over or near the Iberian peninsula. In contrast, the HWs developing under omega blocking exhibit a higher variety in air-mass origin and pathways towards Central Europe. In a lot of cases, the air masses reach the HW region from an easterly direction after traversing Scandinavia before turning anticyclonically over Eastern Europe.

  Close to the surface (10–50 hPa above ground), the origin of HW-related air masses is overall similar, but shifted to the north by some 5° compared with air residing at the top of the PBL. For both ridge- and omega-type HWs, the onset phase is on average characterized by air masses originating from the northern Atlantic region, which are transported rapidly eastwards and only become anomalously warm close to or over the European component after they have descended to levels around 850 hPa. While the overall air-mass pathway is similar during the onset phase, the location at which air masses first show positive temperature anomalies is already significantly further north and east in omega-type HWs compared with ridge-type HWs.

Towards the later HW stages, these differences between both HW types are again more substantial. Air masses in omega-type HWs show a pronounced anticyclonic motion pattern and mostly become anomalously warm somewhere east of the Central European region. In contrast, air masses involved in ridge-type HWs first develop positive temperature anomalies southwest of the Central European region in the majority of cases.

- *Does the relative importance of the processes of advection, adiabatic warming, and diabatic warming differ fundamentally between ridge- and omega-type HWs and does the relative importance of these processes change over the course of the heatwave?*

  Air masses residing at 175–225 hPa above ground level have on average been diabatically cooled on their way to the HW region, and anomalous heat is present due to advection and subsidence-induced adiabatic warming (Figure 12). During the onset phase, subsidence warming dominates, with a relative contribution of around 100% for both ridge- and omega-type HWs. Until HW day 3, the contribution drops to levels of 70% for ridge- and 80% for omega-type HWs. In ridge-type HWs, advection then becomes the most important contributor to anomalously high temperatures at heights around the top of the PBL. With a mean value of around 90%, a significant difference emerges in comparison with omega-type HWs, where the advective fractions remain steady at around 50% over the course of the HWs. The lower relative contribution of advection is reflected in less diabatic cooling in omega-type HWs at the top of the PBL.

  Close to the surface, initially small differences between ridge- and omega-type HWs become more pronounced towards the more mature HW stage. During the onset phase, adiabatic warming and diabatic heating both contribute most strongly with 40%–50% each, but advection also has a share of nearly 20%. In contrast, omega-type HWs feature a significantly lower advective contribution of about 0%, but similar, statistically indistinguishable contributions from adiabatic heating. In turn, the diabatic heating fraction is slightly but significantly elevated compared with ridge-type HWs with a mean of about 50%. Over the course of four HW days investigated, the respective advective contributions stay fairly constant and ridge-type HWs show statistically significant higher advective fractions on three of the four HW days considered. Subsidence-induced warming becomes more dominant, particularly for ridge-type HWs. From HW day 2 onwards, a significant difference develops, with a mean contribution of about 90% for ridge-type HWs compared with 55% in omega-type HWs. Consequently, omega-type HWs are characterized by significantly higher contributions of diabatic warming towards the more mature stage; whereas the diabatic component turns negative at HW day 3 for ridge-type HWs, it stays at around 40% for omega-type HWs.

- *Is there a substantial difference in terms of how diabatic processes in both the free troposphere and the planetary boundary layer affect the air masses involved?*

  On all days beside the day of HW onset, air masses related to omega-type HWs undergo significantly less diabatic cooling in the free troposphere than ridge-type HWs. Moreover, we find increasing differences in the residence time of air parcels within the PBL and over land. On heatwave day 3, air masses associated with omega-type HWs spend on average six hours longer in the PBL and over land, leaving significantly more time for diabatic heating to occur. Other factors beside mere residence time in the PBL, such as short-wave radiation or soil-moisture anomalies along the air-mass path, were not found to differ significantly between omega- and ridge-type HWs.

Despite the overall nuanced picture, with different inferences depending on heatwave stage and the vertical level of the air masses involved, a robust conceptual picture can be drawn for near-surface air masses during the mature HW phase. Consistent with the differences in the large-scale flow field, ridge-type HWs are characterized by a transport of air masses from more southerly and climatologically warmer regions. A considerable part of the temperature anomaly is therefore attributable to horizontal temperature advection, in contrast to omega-type heatwaves, for which this process plays no role on average. Compared with omega-type HWs, air masses involved in ridge-type HWs first become anomalously warm at higher atmospheric levels. While the comparably longer descent equates to a higher contribution of adiabatic warming, it also results in significantly higher diabatic cooling in the free troposphere in comparison with omega-type HWs. These emerging differences in the role of diabatic heating are amplified further as air masses involved in omega-type HWs spend significantly more time within the PBL, resulting in significantly higher diabatic heating from surface heat fluxes and turbulent mixing.

Our results are in line with previous studies and provide an extended understanding of the generation of hot extremes by unravelling the importance of the processes of advection, adiabatic warming, and diabatic heating in relation to the prevalent atmospheric flow anomaly. In particular, we provide novel insight into the variability in the importance of these temperature-modulating rocesses throughout the temporal course of HWs. Despite

differences in methods and scope, the results presented in this study mostly agree with existing literature. With a focus on the hottest days per year, Röthlisberger and Papritz (2023) have shown that in Central Europe heat extremes are on average attributable to positive contributions from all three processes—subsidence, diabatic heating, and advection—with the most important being adiabatic warming. Due to the quantitatively rather small contribution from advection, this is to some extent in line with earlier studies, which suggested that advection is not important for explaining Central European heat extremes (Bieli *et al.*, 2015; Zschenderlein *et al.*, 2019). In agreement with Hotz *et al.* (2024), we also find that the advective fraction becomes much more important when we extend our analysis to air masses higher up in the atmosphere. As a first, Sousa *et al.* (2018) distinguished between subtropical ridges and omega blockings. Using an Eulerian analysis applied to summer days, they attributed a large role to diabatic heating, but identified no substantial differences between both types of large-scale flow anomaly. Focusing on HWs using a Lagrangian framework instead, we have shown that the relative importance of the three heat-generating processes differs significantly between omega-type and ridge-type HW samples, which represent the two most common circulation types during Central European heatwaves well. This may to some extent explain the previously reported high case-to-case variability (Sousa *et al.*, 2020; Zschenderlein *et al.*, 2018) and helps to illuminate the disputed role of advection.

Some limitations apply to the generalizability and interpretability of our results, first and foremost because of the naturally limited sample size. Heatwaves are by definition rare phenomena and, in order to ensure a substantial difference in the large-scale flow evolution, we have chosen to select 25 HWs each from the pool of 216 available HWs. Therefore we do not necessarily focus on particularly severe HWs of high societal impact, although we have excluded the lower quartile of weakest HWs in the selection process. Moreover, our results are not easily generalizable for a considerable number of heatwaves that may feature a transition from an initial ridge phase towards an omega blocking in later stages or large-scale flow configurations not akin to those two canonical types studied. As pointed out in Röthlisberger and Papritz (2023), further caution must be applied when the role of the three heat-generating processes considered is interpreted. For instance, on the one hand a particularly strong diabatic contribution may point to particularly strong diabatic heating from sensible surface fluxes. On the other hand, these fluxes may have been particularly strong due to the advection of a rather cold air mass, and therefore a high "atmospheric demand". However, such cases, which potentially lead to misinterpretation, are to a large extent excluded by the condition that all Lagrangian temperature anomaly contributions are integrated only from the point in time at which an air parcel first became anomalously warm. Finally, the roles of the three different processes may also be viewed not in absolute terms but relative to their climatological mean values. Mayer and Wirth (2024) have shown that advection might indeed be an important factor for explaining the anomalous heat in recent HWs. This is due to the fact that, during summertime, air masses travelling to Central Europe originate mostly from climatologically cooler regions, such that the contribution due to advection is usually negative. Therefore a low advective fraction of around 20%, as shown in this study for ridge-type HWs, might indicate a particularly strong role of advection compared with summer climatology.

In summary, our study provides new insights into the role of different processes in generating anomalously high temperatures over Central Europe. We propose that, in addition to the geographical region and regional factors such as coastlines or orography, the present large-scale circulation may also alter considerably the way in which air masses are heated in a HW. In a future climate, Central European HWs are expected to become more severe, due purely to the thermodynamic contribution from global warming. It is still unclear whether changes in the atmospheric dynamics may also play a considerable role. So far, there are large uncertainties about the expected changes in atmospheric blocking (Davini & d'Andrea, 2020; Lohmann *et al.*, 2024; Woollings *et al.*, 2018). However, northward-extending subtropical ridges, not usually registered by blocking-detection algorithms, may become increasingly important. This is generally in line with the projection of a northward-shifting subtropical anticyclone belt (Gillett & Stott, 2009). Therefore, the mechanisms leading to anomalous heat may also change in a future climate. Hence, it would in our opinion be valuable also to apply Lagrangian methods as used in this article not only to model output from reanalyses or weather forecasts but also to decadal predictions and future climate projections. Finally, by stratifying HWs by intensity rather than atmospheric circulation type, the methods used in this article could also be used to explore the key processes that make a HW particularly extreme, be it in today's climate or in a projected future climate.

ACKNOWLEDGEMENTS

The authors thank the German Climate Computing Center (DKRZ), Hamburg, for providing computing and storage resources under project numbers 1159 and 1152. This study is funded by the German Federal Ministry of Research, Technology, and Space (BMFTR) research program ClimXtreme II: A5 DesAttHeat (Grant number:

01LP2322A). J. G. Pinto thanks the AXA Research Fund. M. M. Lima was supported through the PhD MIT Portugal MPP2030-FCT programme (doi: 10.54499/PRT/BD/154680/2023). The authors thank Ricardo M. Trigo (IDL, Lisbon) for discussions in the initial stages of this research. Finally, all authors appreciate the work of two reviewers and the associate editor, whose valuable comments have contributed significantly to improving the quality and clarity of this article. Open Access funding enabled and organized by Projekt DEAL.

CONFLICTS OF INTEREST STATEMENT

The authors declare no conflicts of interest.

DATA AVAILABILITY STATEMENT

The data that support the findings of this study are available from the corresponding author upon reasonable request.

The ERA5 data used for the detection of heatwaves are provided for the public under the following URL: https://cds.climate.copernicus.eu/cdsapp#!/dataset/reanalysis-era5-single-levels?tab=overview.

The LAGRANTO code for the computation of kinematic backward trajectories is made available under https://iacweb.ethz.ch/staff/sprenger/lagranto/. Python code and further information about the Lagrangian temperature decomposition can be accessed under the following URL: https://www.research-collection.ethz.ch/handle/20.500.11850/571107.

Scripts used to generate the plots of this article can be provided by the corresponding author upon request (alexander.lemburg@kit.edu).

ENDNOTE

[1]In its final stage, atmospheric blocking may also result in a distinctive disturbance or even split of the upper-level air flow, which is commonly referred to as a Rex-type blocking (Rex, 1950). However, during summer, Rex-type blockings are observed only rarely in the midlatitudes (Sousa *et al.*, 2021) and they will not be considered in this article.

ORCID

Alexander Lemburg https://orcid.org/0000-0001-8059-0546
Andreas H. Fink https://orcid.org/0000-0002-5840-2120
Miguel M. Lima https://orcid.org/0000-0003-1433-4805
Joaquim G. Pinto https://orcid.org/0000-0002-8865-1769

REFERENCES

Alvarez-Castro, M.C., Faranda, D. & Yiou, P. (2018) Atmospheric dynamics leading to west European summer hot temperatures since 1851. *Complexity*, 2018, 2494509.

Barriopedro, D., Fischer, E.M., Luterbacher, J., Trigo, R.M. & García-Herrera, R. (2011) The hot summer of 2010: redrawing the temperature record map of Europe. *Science*, 332, 220–224.

Bieli, M., Pfahl, S. & Wernli, H. (2015) A Lagrangian investigation of hot and cold temperature extremes in Europe. *Quarterly Journal of the Royal Meteorological Society*, 141, 98–108.

Davini, P. & d'Andrea, F. (2020) From cmip3 to cmip6: Northern hemisphere atmospheric blocking simulation in present and future climate. *Journal of Climate*, 33, 10021–10038.

Dong, B. & Sutton, R.T. (2025) Drivers and mechanisms contributing to excess warming in Europe during recent decades. *NPJ Climate and Atmospheric Science*, 8, 41.

Fink, A.H., Brücher, T., Krüger, A., Leckebusch, G.C., Pinto, J.G. & Ulbrich, U. (2004) The 2003 European summer heatwaves and drought–synoptic diagnosis and impacts. *Weather*, 59, 209–216.

García-Herrera, R., Díaz, J., Trigo, R. & Hernández, E. (2005) Extreme summer temperatures in Iberia: health impacts and associated synoptic conditions. In: *Annales Geophysicae*, Vol. 23. Göttingen, Germany: Copernicus Publications, pp. 239–251.

García-Herrera, R., Díaz, J., Trigo, R.M., Luterbacher, J. & Fischer, E.M. (2010) A review of the European summer heat wave of 2003. *Critical Reviews in Environmental Science and Technology*, 40, 267–306.

Gillett, N. & Stott, P. (2009) Attribution of anthropogenic influence on seasonal sea level pressure. *Geophysical Research Letters*, 36, L23709.

Hotz, B., Papritz, L. & Röthlisberger, M. (2024) Understanding the vertical temperature structure of recent record-shattering heatwaves. *Weather and Climate Dynamics*, 5, 323–343.

Kautz, L.-A., Martius, O., Pfahl, S., Pinto, J.G., Ramos, A.M., Sousa, P.M. et al. (2022) Atmospheric blocking and weather extremes over the euro-Atlantic sector–a review. *Weather and Climate Dynamics*, 3, 305–336.

Kornhuber, K., Bartusek, S., Seager, R., Schellnhuber, H.J. & Ting, M. (2024) Global emergence of regional heatwave hotspots outpaces climate model simulations. *Proceedings of the National Academy of Sciences*, 121, e2411258121.

Kueh, M.-T. & Lin, C.-Y. (2020) The 2018 summer heatwaves over northwestern Europe and its extended-range prediction. *Scientific Reports*, 10, 19283.

Legg, S. (2021) Ipcc, 2021: Climate change 2021-the physical science basis. *Interaction*, 49, 44–45.

Lemburg, A. & Fink, A.H. (2024) Investigating the medium-range predictability of European heatwave onsets in relation to weather regimes using ensemble reforecasts. *Quarterly Journal of the Royal Meteorological Society*, 150, 3957–3988.

Lima, M.M., Sousa, P.M., Fuentes-Alvarez, T., Ordóñez, C., García-Herrera, R., Barriopedro, D. et al. (2026) Stable: an open-source atmospheric blocking and subtropical ridge detection system. *Environmental Modelling & Software*, 195, 106729.

Lohmann, R., Purr, C. & Ahrens, B. (2024) Northern hemisphere atmospheric blocking in cmip6 climate projections using a hybrid index. *Journal of Climate*, 37, 6605–6625.

Mayer, A. & Wirth, V. (2024) Lagrangian characterization of heat waves: the perspective matters. *EGUsphere*, 2024, 1–29.

Pfahl, S. & Wernli, H. (2012) Quantifying the relevance of atmospheric blocking for co-located temperature extremes in the northern hemisphere on (sub-) daily time scales. *Geophysical Research Letters*, 39, L12807.

Rex, D.F. (1950) Blocking action in the middle troposphere and its effect upon regional climate. *Tellus*, 2, 275–301.

Röthlisberger, M. & Papritz, L. (2023) Quantifying the physical processes leading to atmospheric hot extremes at a global scale. *Nature Geoscience*, 16, 210–216.

Rousi, E., Fink, A.H., Andersen, L.S., Becker, F.N., Beobide-Arsuaga, G., Breil, M. et al. (2023) The extremely hot and dry 2018 summer in central and northern Europe from a multi-faceted weather and climate perspective. *Natural Hazards and Earth System Sciences*, 23, 1699–1718.

Rousi, E., Kornhuber, K., Beobide-Arsuaga, G., Luo, F. & Coumou, D. (2022) Accelerated western European heatwave trends linked to more-persistent double jets over Eurasia. *Nature communications*, 13, 3851.

Sánchez-Benítez, A., Barriopedro, D. & García-Herrera, R. (2020) Tracking Iberian heatwaves from a new perspective. *Weather and Climate Extremes*, 28, 100238.

Santos, J.A., Pfahl, S., Pinto, J.G. & Wernli, H. (2015) Mechanisms underlying temperature extremes in Iberia: a Lagrangian perspective. *Tellus Series A: Dynamic Meteorology and Oceanography*, 67, 26032.

Santos, J.A., Pinto, J.G. & Ulbrich, U. (2009) On the development of strong ridge episodes over the eastern north Atlantic. *Geophysical Research Letters*, 36, L17804.

Schaller, N., Sillmann, J., Anstey, J., Fischer, E.M., Grams, C.M. & Russo, S. (2018) Influence of blocking on northern European and western Russian heatwaves in large climate model ensembles. *Environmental Research Letters*, 13, 054015.

Scherrer, S.C., Croci-Maspoli, M., Schwierz, C. & Appenzeller, C. (2006) Two-dimensional indices of atmospheric blocking and their statistical relationship with winter climate patterns in the euro-Atlantic region. *International Journal of Climatology*, 26, 233–250.

Schumacher, D.L., Singh, J., Hauser, M., Fischer, E.M., Wild, M. & Seneviratne, S.I. (2024) Exacerbated summer European warming not captured by climate models neglecting long-term aerosol changes. *Communications Earth & Environment*, 5, 182.

Singh, J., Sippel, S. & Fischer, E.M. (2023) Circulation dampened heat extremes intensification over the midwest USA and amplified over western Europe. *Communications Earth & Environment*, 4, 432.

Soci, C., Hersbach, H., Simmons, A., Poli, P., Bell, B., Berrisford, P. et al. (2024) The era5 global reanalysis from 1940 to 2022. *Quarterly Journal of the Royal Meteorological Society*, 150, 4014–4048.

Sousa, P.M., Barriopedro, D., García-Herrera, R., Ordóñez, C., Soares, P.M. & Trigo, R.M. (2020) Distinct influences of large-scale circulation and regional feedbacks in two exceptional 2019 European heatwaves. *Communications Earth & Environment*, 1, 1–13.

Sousa, P.M., Barriopedro, D., García-Herrera, R., Woollings, T. & Trigo, R.M. (2021) A new combined detection algorithm for blocking and subtropical ridges. *Journal of Climate*, 34, 7735–7758.

Sousa, P.M., Barriopedro, D., Ramos, A.M., García-Herrera, R., Espírito-Santo, F. & Trigo, R.M. (2019) Saharan air intrusions as a relevant mechanism for Iberian heatwaves: The record breaking events of august 2018 and June 2019. *Weather and Climate Extremes*, 26, 100224.

Sousa, P.M., Trigo, R.M., Barriopedro, D., Soares, P.M. & Santos, J.A. (2018) European temperature responses to blocking and ridge regional patterns. *Climate Dynamics*, 50, 457–477.

Sprenger, M. & Wernli, H. (2015) The Lagranto Lagrangian analysis tool–version 2.0. *Geoscientific Model Development*, 8, 2569–2586.

Stegehuis, A.I., Vogel, M.M., Vautard, R., Ciais, P., Teuling, A.J. & Seneviratne, S.I. (2021) Early summer soil moisture contribution to western European summer warming. *Journal of Geophysical Research: Atmospheres*, 126, e2021JD034646.

Tibaldi, S. & Molteni, F. (1990) On the operational predictability of blocking. *Tellus. Series A, Dynamic Meteorology and Oceanography*, 42, 343–365.

Vautard, R., Cattiaux, J., Happé, T., Singh, J., Bonnet, R., Cassou, C., Coumou, D., D'Andrea, F., Faranda, D., Fischer, E. et al. (2023) Heat extremes in western Europe are increasing faster than simulated due to missed atmospheric circulation changes review. Available from: https://doi.org/10.21203/rs-3.

Woollings, T., Barriopedro, D., Methven, J., Son, S.-W., Martius, O., Harvey, B. et al. (2018) Blocking and its response to climate change. *Current climate change reports*, 4, 287–300.

Zschenderlein, P., Fink, A.H., Pfahl, S. & Wernli, H. (2019) Processes determining heat waves across different European climates. *Quarterly Journal of the Royal Meteorological Society*, 145, 2973–2989.

Zschenderlein, P., Fragkoulidis, G., Fink, A.H. & Wirth, V. (2018) Large-scale rossby wave and synoptic-scale dynamic analyses of the unusually late 2016 heatwave over Europe. *Weather*, 73, 275–283.

SUPPORTING INFORMATION

Additional supporting information can be found online in the Supporting Information section at the end of this article.

How to cite this article: Lemburg, A., Fink, A.H., Lima, M.M. & Pinto, J.G. (2026) Lagrangian analysis of two flavours of Central European heatwaves: Formation under omega blocking versus initiation by subtropical ridges. *Quarterly Journal of the Royal Meteorological Society*, e70199. Available from: https://doi.org/10.1002/qj.70199